Impact of lattice strangeness asymmetry data in the CTEQ-TEA global analysis

Tie-Jiun Hou,[1,*] Huey-Wen Lin,[2,3,†] Mengshi Yan,[4,‡] and C.-P. Yuan[2,§]

[1]*School of Nuclear Science and Technology, University of South China, Hengyang, Hunan 421001, China*
[2]*Department of Physics and Astronomy, Michigan State University, East Lansing, Michigan 48824, USA*
[3]*Department of Computational Mathematics, Science and Engineering, Michigan State University, East Lansing, Michigan 48824, USA*
[4]*Department of Physics and State Key Laboratory of Nuclear Physics and Technology, Peking University, Beijing 100871, China*

(Received 14 December 2022; accepted 4 April 2023; published 21 April 2023)

We study the impact of lattice data on the determination of the strangeness asymmetry distribution $s_-(x) \equiv s(x) - \bar{s}(x)$ in the general CTEQ-TEA global analysis of parton distribution functions (PDFs) of the proton. Firstly, we find that allowing a nonvanishing $s_-(x)$, at the initial $Q_0 = 1.3$ GeV scale, in a global PDF analysis leads to a CT18As fit with similar quality to CT18A. Secondly, including the lattice data in the CT18As_Lat fit greatly reduces the s_--PDF error band size in the large-x region. To further reduce its error would require more precise lattice data, extended to smaller x values. We take ATLAS 7 TeV W and Z production data, SIDIS dimuon production data, F_3 structure function data, E866 NuSea data, and E906 SeaQuest data as examples to illustrate the implication of CT18As and CT18As_Lat fits. The parametrization dependence for PDF ratio $(s+\bar{s})/(\bar{u}+\bar{d})(x)$ is analyzed with CT18As2 and CT18As2_Lat fits as results.

DOI: 10.1103/PhysRevD.107.076018

I. INTRODUCTION

The Large Hadron Collider (LHC) has entered an era of precision physics. To match the experimental precision, it is necessary to have precise predictions in QCD theory, which require correspondingly precise parton distribution functions (PDFs), such as the recent CT18 [1], MSHT20 [2] and NNPDF4.0 [3] PDFs obtained at the next-to-next-to-leading order (NNLO) accuracy in QCD. Generally speaking, while the up- and down-(anti)quark PDFs of the proton have been well-determined, for x between 10^{-4} and 0.4, the strange quark and antiquark distribution functions still remain uncertain. Many efforts [4–7] have been dedicated to the determination of the strange (anti) quark PDF with constraints from fixed-target and collider experimental data.

In the CT18 analysis, the strange quark and antiquark PDFs of the proton are assumed to be the same, $\bar{s}(x) = s(x)$, at $Q_0 = 1.3$ GeV, where the nonperturbative PDFs are specified, and a nonvanishing $(s-\bar{s})(x)$ is generated at higher-energy scales by DGLAP evolution [8,9]. In Ref. [1], noticeable tensions between the original NuTeV [10] and CCFR [11] semi-inclusive deep-inelastic scattering (SIDIS) dimuon data and the precision ATLAS $\sqrt{s} = 7$ TeV W, Z data [12] were found. In MSHT20 [2], it was concluded that allowing $s(x) \neq \bar{s}(x)$ at the Q_0 scale can release some of these tensions. In this work, we extend the CT18 analysis to allow a nonvanishing strangeness asymmetry, $s_-(x) \equiv s(x) - \bar{s}(x)$, at the Q_0 scale, and the resulting PDF set is hereafter referred to as CT18As.

Besides the phenomenology approach of performing global PDF analysis, a nonperturbative approach from first principles, such as lattice QCD (LQCD), provides hope to resolve many of the outstanding theoretical disagreements and provides information in regions that are unknown or difficult to observe in experiments. Recent breakthroughs, such as large-momentum effective theory (LaMET) [13–15] (also called the quasi-PDF method), have made it possible for lattice calculations to provide information on the x-dependent PDFs. There have been many pioneering works showing great promise in obtaining quantitative results for the unpolarized, helicity, and transversity quark and antiquark distributions [16–21] using the quasi-PDFs

*tjhou@msu.edu
†hueywen@msu.edu
‡msyan@pku.edu.cn
§yuanch@msu.edu

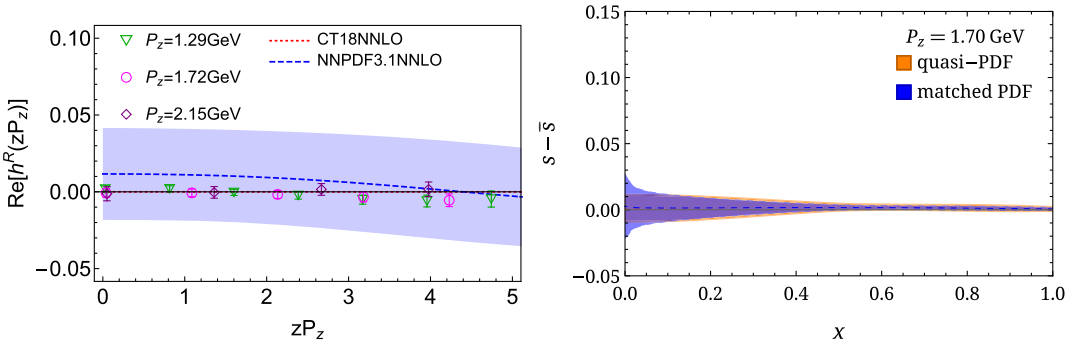

FIG. 1. (left) The real parts of the strange quasi-PDF matrix elements in coordinate space from our calculations at physical pion mass with $P_z \in [1.3, 2.15]$ GeV [25], along with those from CT18 and NNPDF NNLO. (right) The quasi (orange) and matched (blue) valence strange distribution from LQCD calculation.

approach [13]. Increasingly many lattice works are being performed at physical pion mass since the first study in Ref. [22]. (A recent review of the theory and lattice calculations can be found in Refs. [15,23,24].) The first Bjorken x-dependent strange (anti)quark PDF using LQCD calculations was reported in Ref. [25]. This calculation was done using a single-lattice spacing, 0.12 fm, with extrapolation to physical pion masses. In this work, we use the extrapolated lattice matrix elements to calculate the strangeness asymmetry distribution $s_-(x) \equiv s(x) - \bar{s}(x)$, which is then taken as an input to further constrain $s(x)$ and $\bar{s}(x)$ at the Q_0 scale in the CT18-like global analysis. The resulting PDF set is denoted as CT18As_Lat.

The strangeness asymmetry $s_-(x)$ in the lattice calculation and the CTEQ-TEA PDF analysis is reviewed in Sec. II. Section III describes the updated strangeness asymmetry results obtained in CT18As and CT18As_Lat fits, by allowing a nonvanishing strangeness asymmetry $s_-(x)$ at the initial $Q_0 = 1.3$ GeV scale. The implication of CT18As and CT18As_Lat fits is studied in Sec. IV by comparing numerical predictions to experimental data for some observables. Section V contains our conclusion. In Appendix A, we study the parametrization dependence of the PDF ratio $(s+\bar{s})/(\bar{u}+\bar{d})(x)$ in the large-x region and obtain alternative CT18As2 and CT18As2_Lat PDFs. In Appendix B, we summarize the specific parametrization functional forms for $s(x)$ and $\bar{s}(x)$ PDFs.

II. STRANGENESS ASYMMETRY FROM LATTICE AND CT18

A. Lattice calculation of the strangeness asymmetry distribution $s_-(x)$

Since the strangeness asymmetry $s_-(x) \equiv s(x) - \bar{s}(x)$ is flavor-singlet, we can confidently calculate it using LaMET coordinate-space matrix elements on the lattice. In this work, we use the matrix elements from Ref. [25] computed on a single 0.12 fm lattice ensemble with a $(2+1+1)$-flavor highly-improved staggered quarks (HISQ) sea with 310 MeV pions generated by MILC Collaboration [26,27]. The calculation uses two valence masses for the nucleon; light ($M_\pi \approx 310$ MeV) and strange ($M_\pi \approx 690$ MeV). The two-point correlators include 344,064 and 57,344 measurements, respectively, and are extrapolated to the physical pion mass. The matrix elements are renormalized using the nonperturbative renormalization (NPR) in RI/MOM scheme, the same strategy as in previous works [28,29]. The left-hand side of Fig. 1 shows the lattice real matrix elements at $M_\pi = 135$ MeV (extrapolated linearly in M_π^2) with nucleon boost momenta $P_z \in [1.3, 2.2]$ compared with the CT18 NNLO (red band with dot-dashed line) and NNPDF3.1 NNLO (orange band with dotted line) gluon PDFs. The real matrix elements are proportional to the integral of the difference between strange and antistrange PDFs $[\int dx(s(x) - \bar{s}(x))\cos(xzP_z)]$, where z is the Wilson-line displacement, as shown in Fig. 2 of Ref. [25]. The lattice results of the real quasi-PDF matrix elements, as shown in Fig. 1, are consistent with zero at 95% confidence level for most zP_z points, indicating that the strange quark-antiquark asymmetry is likely very small.

To take advantage of existing lattice data to reach a wider region of x, we choose to focus on the result of $P_z \approx 1.7$ GeV. We Fourier transform the renormalized matrix elements into quasi-PDFs by using the extrapolation formulation suggested in Ref. [30] to fit the large-$|z|$ data to the formula $c_1(-izP_z)^{-d_1} + c_2 e^{izP_z}(izP_z)^{-d_2}$, inspired by the Regge behavior. Extrapolating the matrix elements into the region beyond the lattice calculation then suppresses Fourier-transformation artifacts. The quasi-PDF can be related to the P_z-independent light cone PDF at scale μ in $\overline{\text{MS}}$ scheme through a factorization theorem [14]

$$\tilde{q}_\psi(x, P_z, \mu^{\overline{\text{MS}}}, \mu^{\text{RI}}, p_z^{\text{RI}}) = \int_0^1 \frac{dy}{|y|} C\left(\frac{x}{y}, \left(\frac{\mu^{\text{RI}}}{p_z^{\text{RI}}}\right)^2, \frac{yP_z}{\mu^{\overline{\text{MS}}}}, \frac{yP_z}{p_z^{\text{RI}}}\right) q_\psi(y, \mu^{\overline{\text{MS}}}) + \cdots, \quad (1)$$

where p_z^{RI} and μ^{RI} are the momentum of the off shell strange quark, and the renormalization scale in the RI/MOM-scheme

nonperturbative renormalization, C is a perturbative matching kernel used in our previous works [31–34]. The quasi and matched strangeness asymmetry distributions as functions of x can be found on the right-hand side of Fig. 1; both are consistent with zero. Note that the matching from quasi-PDF to PDF has residual systematics at $O(\frac{\Lambda^2_{\rm QCD}}{(xP_z)^2})$ and $O(\frac{\Lambda^2_{\rm QCD}}{(1-x)^2P_z^2})$ at very small x and x near 1, respectively. From the isovector nucleon PDF study, at this P_z boost momentum, we can reasonably rely on lattice x-dependent strange asymmetry for $x \in [0.3, 0.8]$ with interval of 0.01 jackknife sampling. Beyond this region, the lattice errors could increase significantly due to the systematics at finite momentum.

B. Strangeness asymmetry $s_-(x)$ in CTEQ-TEA PDF analysis

In the nominal CTEQ-TEA PDF fit [1,35–38], the active parton flavors to be parametrized at $Q_0 = 1.3$ GeV are u, $\bar{u}$, d, $\bar{d}$, s, $\bar{s}$, and g. In the parametrization of sea-quark distributions, $s(x, Q_0) = \bar{s}(x, Q_0)$ is imposed in the nominal CT PDFs. In contrast, the CTEQ6.5S0 PDF [38] and its earlier version [39], done at the NLO, focus on the strangeness sector, where the strangeness asymmetry $s_-(x, Q_0)$ is explicitly parametrized at Q_0.

In this work, we follow the strategy presented in Ref. [38] to perform a global PDF analysis with nonzero $s_-(x, Q_0)$, but with updated experimental data and nonperturbative parametrization forms of active partons at the Q_0 scale, together with NNLO theory predictions. The resulting PDF set is denoted as "CT18As". More specifically, in the CT18As analysis, we start from the alternative PDF set, CT18A NNLO [1], rather than the nominal CT18 NNLO fit. This is because the ATLAS $\sqrt{s} = 7$ TeV W, Z combined cross section measurement [12] (ID = 248) data set is included in the CT18A fit, while it is absent in the nominal CT18 fit. In the analysis of CT18A, this data is found to prefer larger total strangeness, $s_+ \equiv s(x) + \bar{s}(x)$ in the small-x region, and to have tensions with other dimuon data [10], which is sensitive to the strangeness distribution.

The CT18As fit adopts the same nonperturbative PDF forms as the CT18A fit at the Q_0 scale, except for the strange quark and antiquark PDFs, which are determined by $s_+(x)$ and $s_-(x)$. The parametrization of the strangeness asymmetry distribution $s_-(x)$ should respect the number sum rule for strangeness,

$$\int_0^1 dx\, s_-(x) = \int_0^1 dx\, s(x) - \bar{s}(x) = 0. \tag{2}$$

In principle, a parametrization with any number of crossings, with $s_-(x) = 0$, is possible, as long as Eq. (2) is satisfied. Here, we focus on parametrization forms with only one crossing in the range $x \in [10^{-6}, 1]$.

To obtain CT18As_Lat PDFs, we take the lattice data for the strangeness asymmetry presented in Sec. II A as a constraint to the global PDF fit. We use the Lagrange multiplier method [40], since we regard the lattice $s_-(x)$ results as additional data on top of the CT18A data set. Hence, CT18As_Lat is an update to CT18As with the inclusion of the lattice $s_-(x)$ data evaluated at the Q_0 scale.

TABLE I. The total goodness-of-fit $\chi^2_{\rm tot}$ of the CT18A, CT18As, and CT18As_Lat fits, respectively, at $Q_0 = 1.3$ GeV. The total number of data points (without including the lattice data) of each fit is 3674.

PDF	$s_-(x, Q_0)$	Lattice data	$\chi^2_{\rm tot}$
CT18A	0	No	4376
CT18As	$\neq 0$	No	4344
CT18As_Lat	$\neq 0$	Yes	4361

III. UPDATED STRANGENESS ASYMMETRY RESULTS

In this section, we discuss the quality of various fits and compare the resulting PDFs. The qualities of the CT18A, CT18As, and CT18As_Lat fits are compared in Table I, which shows that they all have the similar χ^2, meaning that these three PDFs are comparable in describing the experimental data. The difference in their $\chi^2_{\rm tot}$ is much smaller than the tolerance (with a difference of 100 units) used in the CT18 analysis to define the PDF uncertainty at the 90% confidence level (CL).

We present the qualities of fit of each individual data set E by comparing the effective Gaussian variable $S_E = \sqrt{2\chi^2_E} - \sqrt{2N_{{\rm pt},E} - 1}$ in Fig. 2 (see Ref. [1] and references therein). Alternative to the usual χ^2, the effective Gaussian variable provides an estimation of quality of fit. $S_E > 1$ means that data set E is not fitted well, while $S_E < 1$ represents overfitting. Moreover, if all deviations of theory from data are purely of random fluctuation, the distribution of S_E is expected to recover the standard normal distribution $\mathcal{N}(0, 1)$. In Fig. 2, variation of the effective Gaussian variable S_E for individual data sets E suggests the potential sensitivity of the strangeness asymmetry to the data set E. There are three groups of data that show variations in S_E: 1) NuTeV [10] and CCFR [11] SIDIS dimuon production measurements (ID = 124–127), which directly probe (anti) strange PDFs; 2) CDHSW [41] (ID = 109) and CCFR [42] (ID = 111) measurements of the F_3 structure function, which are directly related to the valence-sector PDFs, so to the strangeness asymmetry $s_-(x)$; 3) data sets, which are sensitive to sea-quark PDFs, such as LHC DY data sets, E866 NuSea $Q^3 d^2\sigma_{pp}/(dQdx_F)$ data [43] (ID = 204) and E906 SeaQuest data [44] (ID = 206). A detailed comparison of theory prediction and data for the above mentioned groups of data will be deferred to Sec. IV. For the last group, we pick the ATLAS 7 TeV W and Z differential

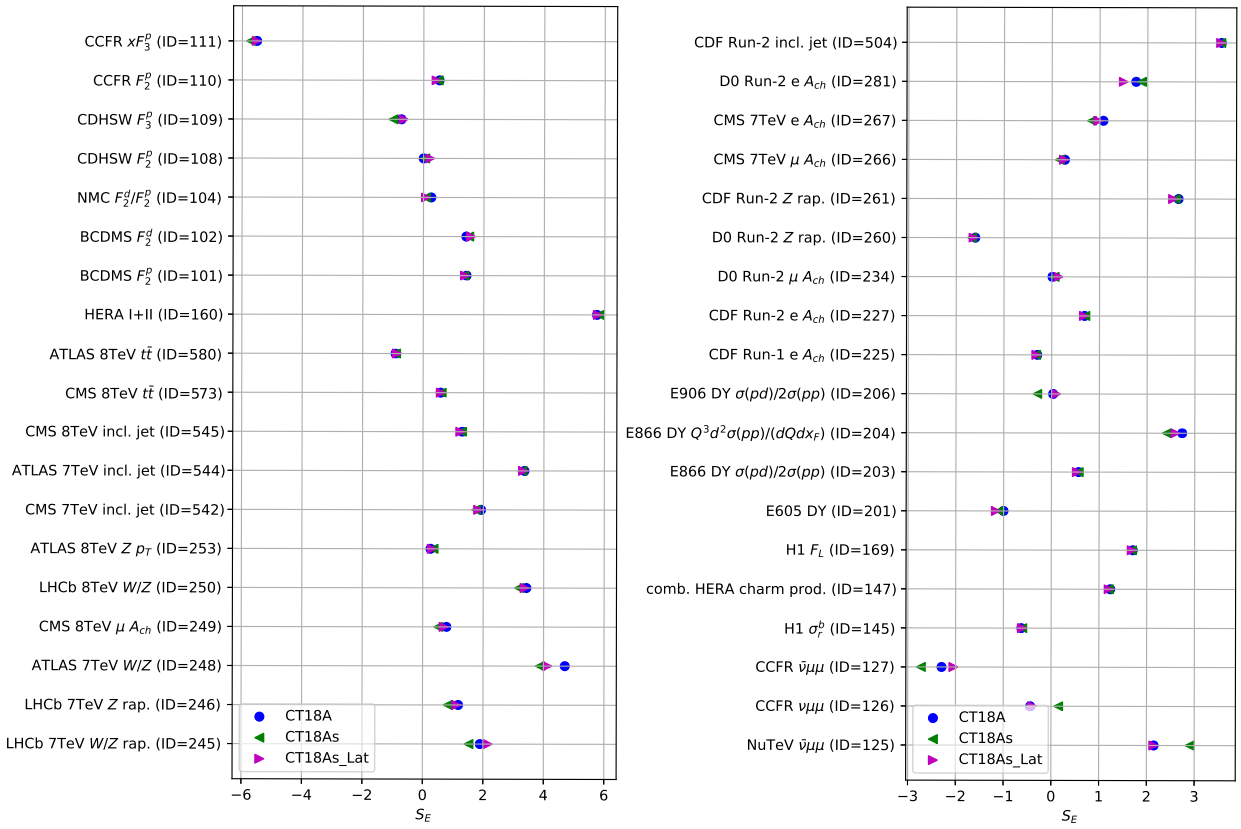

FIG. 2. The effective Gaussian variables S_E for individual data sets included in these fits. The data indices "ID" are as defined in Tables I and II from the prior CT18 study [1]. Note that S_E for the E906 SeaQuest data [44] (ID = 206) is predicted in the above plot but not included in the PDF fits for this study, nor for the nominal CT18 PDF fit.

cross-section measurement [12] (ID = 248) and E906 SeaQuest data [44] (ID = 206) as the representatives. In addition to these groups, the HERA I + II reduced cross section data [45] (ID = 160), as marked in Fig. 2, receives negligible impacts from varying prescriptions of the strangeness asymmetry. Similar to Fig. 2, the quality of fit, χ^2, for the selected data sets in CT18A, CT18As, and CT18As_Lat fits with non-negligible variations in χ^2 is presented in Table II.

Before proceeding, we note that, in the CT18As and CT18As_Lat PDF fits, the charged-current NNLO QCD correction for SIDIS processes [54] is taken into account, in contrast to the original CT18 and CT18A fits [1]. As noted in Sec. V. 4 of the CT18 paper [1], the NNLO prediction provides a marginally better agreement with the data.

The $s_-(x)$ distributions at 2.0 GeV and 100 GeV, and $s(x)$ and $\bar{s}(x)$ at 2.0 GeV of CT18As are compared to PDF fitting results by other groups, as shown in Fig. 3. As shown in the top panels, CT18As agrees with MSHT20 [2] in terms of the s_- central values. For $x \sim 0.1$, NNPDF4.0 [3] presents the largest $s_-(x)$ central value. In the range of $0.05 < x < 0.4$, CT18As shows a wide error band, so that CT18As is consistent with $s_-(x)$ PDF obtained by other groups. For $s(x)$ and $\bar{s}(x)$ PDFs at 2.0 GeV on the bottom panels, three PDFs are in agreement for $x < 0.3$. For $x > 0.3$, three PDFs present different shapes and the CT18As lies in the middle of the MSHT20 [2] and NNPDF4.0 [3] NNLO PDFs.

We compare CT18A, CT18As, and CT18As_Lat at the initial Q_0 scale for $s(x)$, $\bar{s}(x)$, and $s_-(x)$, as well as $s_+(x)$ and PDF ratio $(s+\bar{s})/(\bar{u}+\bar{d})(x)$ at $Q = 100$ GeV in Fig. 4. In the top panels of Fig. 4, we compare $s(x)$ and $\bar{s}(x)$ at the initial scale, among CT18A, CT18As, and CT18As_Lat PDFs. Moving from CT18A to CT18As, allowing a nonvanishing strangeness asymmetry $s_-(x)$ at the initial scale enhances the $s(x)$ PDF but affects $\bar{s}(x)$ less significantly. As the constraint of the lattice data tightens, the CT18As_Lat $s(x)$ PDF becomes closer to that of CT18A. It is appears that the error bands of $s(x)$ and $\bar{s}(x)$ PDFs for CT18As and CT18As_Lat allow a negative value for these PDFs. However, we note that in the parametrization of $s(x)$ and $\bar{s}(x)$ PDFs, cf. Appendix B, we force $s(x)$ and $\bar{s}(x)$ to be non-negative across the whole x range. We checked that these error bands allowing a negative PDF is due to the numerical construction of the Hessian uncertainty, and that all eigenvector PDFs are non-negative. In the middle-left panel of Fig. 4, the impact of lattice data on the strangeness asymmetry $s_-(x)$ is

TABLE II. The χ^2 of selected data sets included in CT18A, CT18As, and CT18As_Lat fits with non-negligible changes in χ^2. The $N_{\mathrm{pt},E}$ is the number of data points for the individual data set E. Note that the E906 SeaQuest data [44] (ID = 206) is not included in PDF fits for this study, as well as the nominal CT18 PDF fit; its χ^2 values are just predicted by the corresponding PDFs. In the bottom row, we also include the χ^2 values of the lattice QCD data in these three PDF fits.

ID	Experimental data set	$N_{\mathrm{pt},E}$	CT18A	CT18As	CT18As_Lat
245	LHCb 7 TeV W/Z rapidity [46]	33	50.1	46.2	50.6
246	LHCb 8 TeV $Z \to ee$ rapidity [47]	17	24.0	21.6	23.3
248	ATLAS 7 TeV 4.6 fb^{-1} W/Z combined cross section [12]	34	87.5	75.6	83.7
249	CMS 8 TeV WA_{ch} [48]	11	14.3	12.9	14.2
250	LHCb 8 TeV W/Z rapidity [49]	34	69.6	66.4	68.7
109	CDHSW F_3^p [41]	96	85.6	82.2	85.3
111	CCFR xF_3^p [42]	86	32.0	30.7	31.8
124	NuTeV $\nu\mu\mu$ SIDIS [10]	38	31.9	29.3	30.2
125	NuTeV $\bar{\nu}\mu\mu$ SIDIS [10]	33	52.8	61.5	53.3
126	CCFR $\nu\mu\mu$ SIDIS [11]	40	35.6	40.7	34.8
127	CCFR $\bar{\nu}\mu\mu$ SIDIS [11]	38	20.9	18.5	20.6
204	E866 Drell-Yan process $Q^3 d^2\sigma_{pp}/(dQdx_F)$ [43]	184	240.8	233.5	240.5
206	E906 Drell-Yan process $\sigma_{pd}/(2\sigma_{pp})$ [44]	6	5.5	4.5	5.0
234	D0 Run-2 muon A_{ch}, $p_{Tl} > 20$ GeV [50]	9	8.4	8.6	8.4
266	CMS 7 TeV 4.7 fb^{-1}, muon A_{ch} $p_{Tl} > 35$ GeV [51]	11	11.6	11.1	11.7
267	CMS 7 TeV 840 pb^{-1}, electron A_{ch} $p_{Tl} > 35$ GeV [52]	11	16.0	14.6	16.1
281	D0 Run-2 9.7 fb^{-1} electron A_{ch}, $p_{Tl} > 25$ GeV [53]	13	23.2	24.1	23.1
	Lattice QCD data of $s_-(x, Q = 1.3\ \mathrm{GeV})$	60	13.25	499.10	1.58

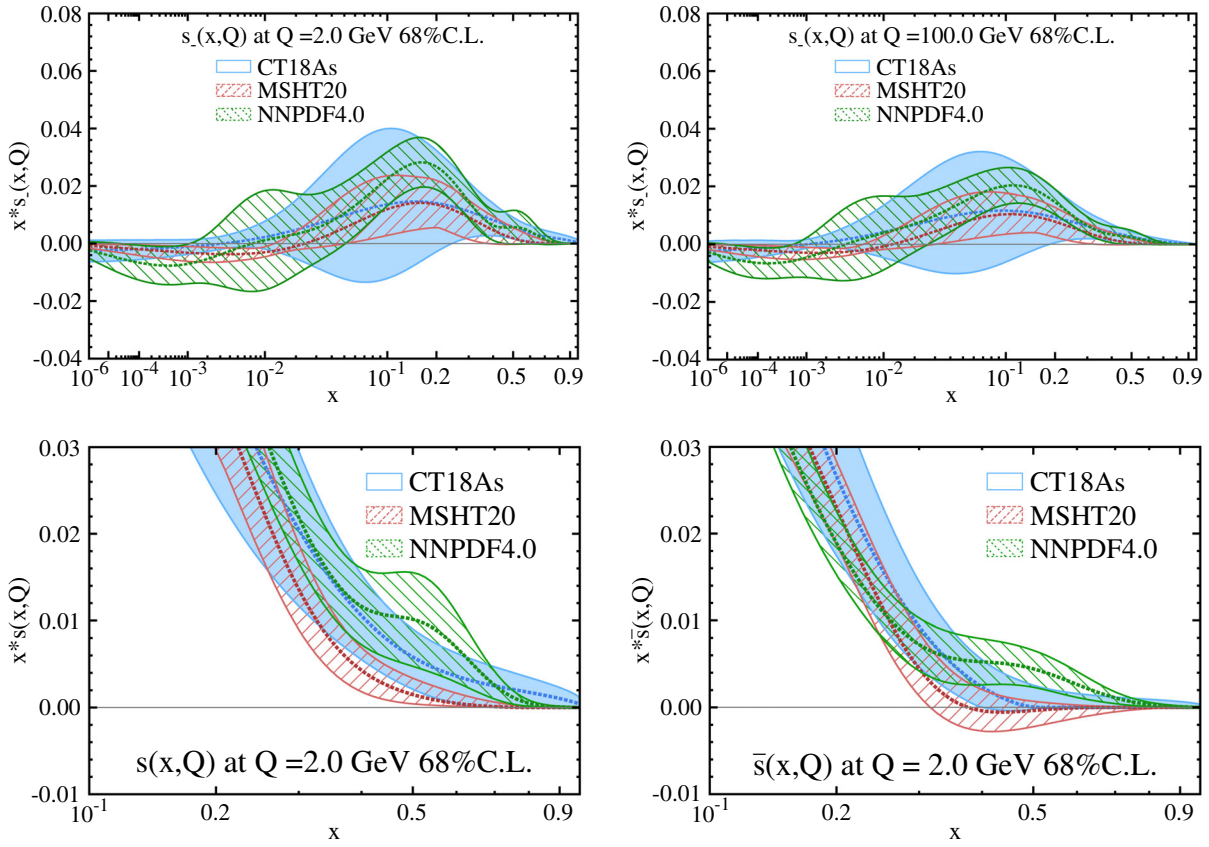

FIG. 3. The CT18As $s_-(x)$ distributions at 2 GeV (top left), 100 GeV (top right), $s(x)$ at 2 GeV (bottom left) and $\bar{s}(x)$ at 2 GeV (bottom right) are compared to those of MSHT20 [2] and NNPDF4.0 [3].

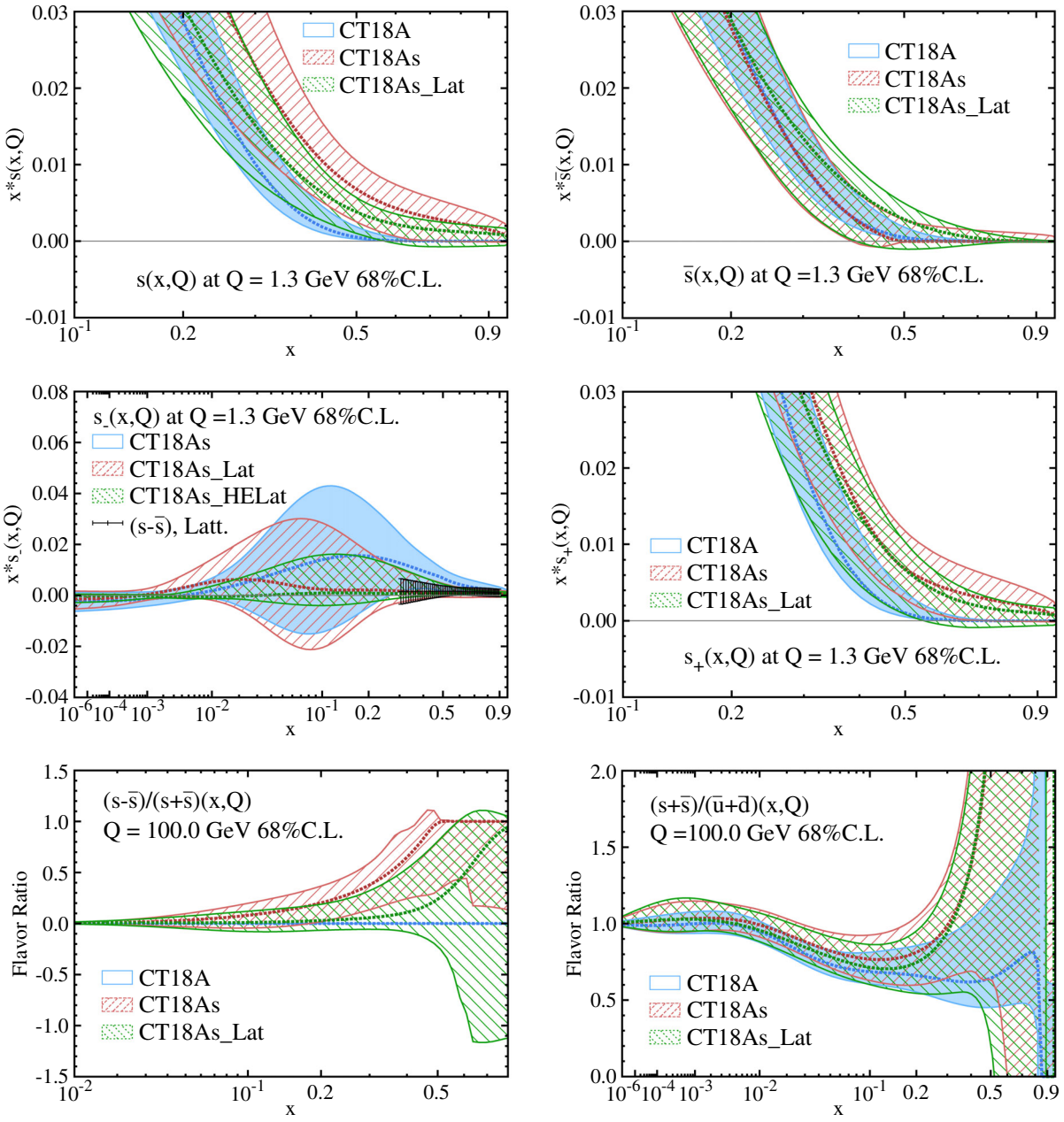

FIG. 4. The comparison of $s(x)$ (top left), $\bar{s}(x)$ (top right), and $s_-(x)$ (middle left), $s_+(x)$ (middle right) PDFs at the initial Q_0 scale, as well as PDF ratios $(s+\bar{s})/(\bar{u}+\bar{d})(x)$ (bottom left) and $(s+\bar{s})/(s-\bar{s})(x)$ (bottom right) at $Q = 100$ GeV, for CT18A, CT18As, and CT18As_Lat. Note that in the middle-left panel, predictions of the strangeness asymmetry of CT18A and CT18As_Lat are compared to the current lattice data and expected improvement if current lattice data errors are reduced by a half (green backslashed area, i.e., CT18As_HELat). For CT18A, no strangeness asymmetry $s_-(x)$ is allowed at the initial Q_0 scale in the nonperturbative parametrization, so CT18A is absent in the comparison plot of $s_-(x)$.

exhibited. The lattice data points are distributed in the region of $0.8 \geq x \geq 0.3$, and they are consistent with a very small strangeness asymmetry with high precision. Compared to the error band of CT18As, the uncertainty in lattice data points is quite small, so that including the lattice data in the CT18As_Lat fit greatly reduces the size of the s_--PDF error band in the large-x region. The amount of reduction of the CT18As_Lat error band in the much smaller x region is likely to depend on the chosen nonperturbative parametrization form of $s_-(x)$ at $Q_0 = 1.3$ GeV. Hence, it is important to have more precise lattice data, extended to smaller x values. Based on the CT18As_Lat PDF, we further investigate how much the lattice data with higher precision would be able to constrain the s_- distribution. We again fit the lattice data, but reduce the uncertainty of lattice data points by half, resulting another

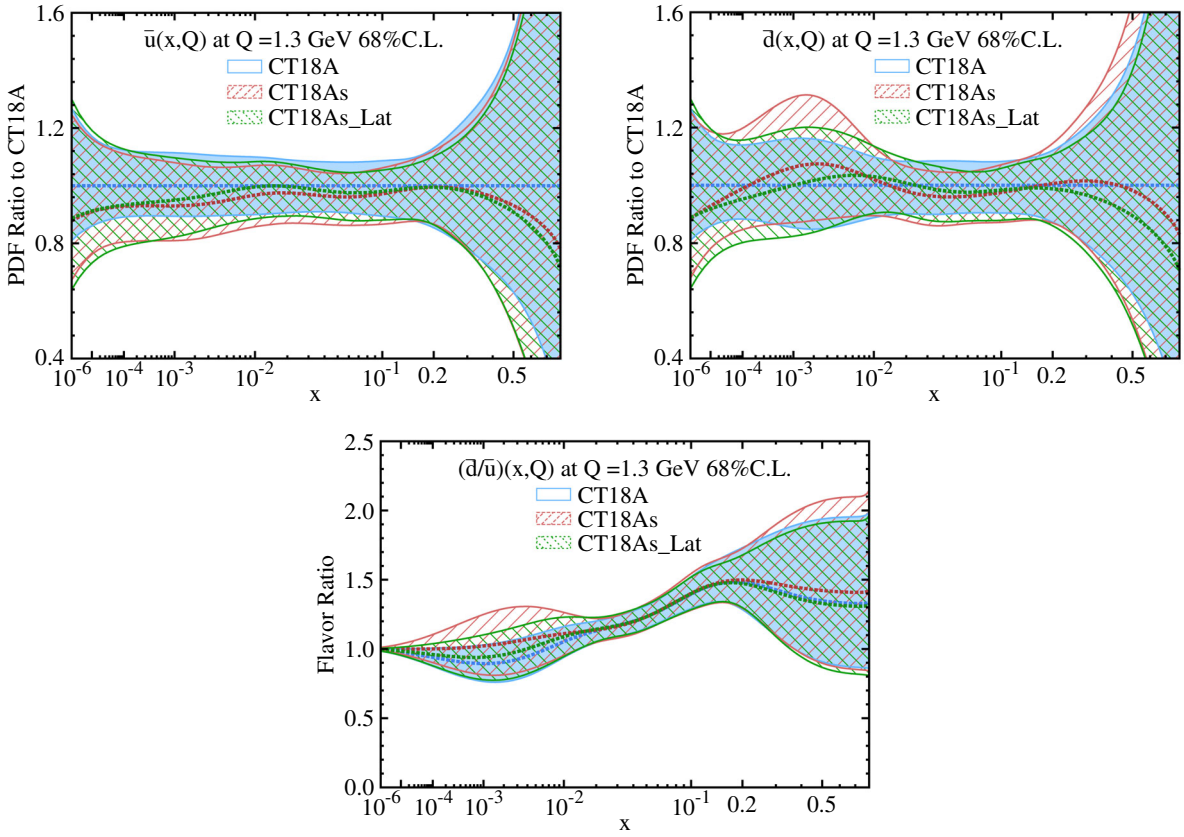

FIG. 5. The comparison of $\bar{u}(x)$ (upper left), $\bar{d}(x)$ (upper right), and $\bar{d}/\bar{u}(x)$ (bottom) parton distributions from the CT18A, CT18As, and CT18As_Lat analyses at the initial Q_0 (= 1.3 GeV) scale.

PDF labeled "CT18As_HELat". The half-error lattice data shows strong power in further constraining s_-, reducing the error band of s_- by nearly a factor of two in the large-x region.[1] In the middle-right panel, the comparison of the total strangeness $s_+(x)$ at $Q_0 = 1.3$ GeV is shown. In CT18As, the central value of the total strangeness $s_+(x)$ is enhanced across a wide range of x relative to CT18A. The uncertainty of s_+ in CT18As is also enlarged. The similar behavior can also be observed in the ratios of strange asymmetry to total strangeness s_-/s_+ and total strangeness to light quarks $(s+\bar{s})/(\bar{u}+\bar{d})(x)$ at $Q = 100$ GeV, as shown in the bottom panel of Fig. 4. Despite of the large uncertainty of the PDF ratio $(s+\bar{s})/(\bar{u}+\bar{d})(x)$ in the large-x region, the enhancement of $(s+\bar{s})/(\bar{u}+\bar{d})(x)$ in CT18As suggests a greater total strangeness than light-quark content. This feature is caused by the choice of the more flexible nonperturbative parametrization form of the (anti)strange PDF adopted in the CT18As fit, as compared to that in CT18. In Appendix A, we present the result of an alternative fit (termed CT18As2 fit) with additional theory prior to constrain the ratio of $(s+\bar{s})/(\bar{u}+\bar{d})(x)$ in the limit of x approaching to 1. After including the lattice data, the resulting CT18As2_Lat fit leads to similar conclusions as the CT18As_Lat fit.

In Fig. 5, we compare the $\bar{u}(x)$, $\bar{d}(x)$, and $\bar{d}/\bar{u}(x)$ PDFs at the initial $Q_0 = 1.3$ GeV. The $\bar{u}(x)$ of CT18As has been decreased for $x < 0.1$ and $x > 0.3$ compared to the $\bar{u}(x)$ of CT18A, as shown in the top-left panel of Fig. 5. After adding in the lattice data, the $\bar{u}(x)$ of CT18As_Lat moves closer to that of CT18A for $0.01 < x < 0.1$, while in the large-x region, CT18As_Lat still has a smaller magnitude in $\bar{u}(x)$. We also observe in the top-right panel of Fig. 5 that $\bar{d}(x)$ of CT18As for $0.01 < x < 0.1$ and $\bar{d}(x)$ of CT18As_Lat for $x > 0.2$ are suppressed in comparison to $\bar{d}(x)$ of CT18A, while they are enhanced at x around a few 10^{-3}. Combining variations in $\bar{u}(x)$ and $\bar{d}(x)$, the PDF ratio $\bar{d}/\bar{u}(x)$ of CT18As floats up for $x > 0.2$ or x around a few 10^{-3}, as shown in the bottom panel.

Lastly in Table III, we summarize the second and third moments of the strangeness asymmetry s_- and the total strangeness s_+ obtained in our phenomenological PDF fits and LQCD calculations. For $\langle x \rangle_{s_+}$ at 2.0 GeV, phenomenological calculations from PDF fits are

[1]To further improve the uncertainties in lattice calculation, we anticipated a future calculation using smaller lattice spacing (say, $a < 0.1$ fm) and higher-boost momenta (preferably with $P_z > 2$ GeV), in addition to reducing the statistical error in the lattice calculations.

TABLE III. The second and the third moments of the strangeness asymmetry s_- and the total strangeness s_+ from phenomenological PDF fits and LQCD calculations (from ETMC [55] and χQCD [56]) at 1.3 (top panel) and 2.0 (bottom panel) GeV. The uncertainty corresponds to 68% confidence level. Of these moments, $\langle x\rangle_{s_+}$ and $\langle x^2\rangle_{s^-}$ are calculable in lattice QCD.

$Q = 1.3$ GeV	CT18A	CT18As	CT18As_Lat	
$\langle x\rangle_{s_-}$	0.0	0.0074(112)	0.0016(70)	
$\langle x^2\rangle_{s_-}$	0.0	0.0024(27)	0.00057(120)	
$\langle x\rangle_{s_+}$	0.038(12)	0.048(19)	0.044(18)	
$\langle x^2\rangle_{s_+}$	0.0035(17)	0.0060(33)	0.0051(30)	
$Q = 2.0$ GeV	CT18A	CT18As	CT18As_Lat	LQCD
$\langle x\rangle_{s_+}$	0.043(10)	0.052(17)	0.048(16)	0.052(12) [55] 0.051(26)(5) [56]

consistent with the recent LQCD calculations by ETMC [55] and χQCD [56] using the traditional moment method.

IV. PHENOMENOLOGY

In this section, we illustrate the impact of allowing nonzero strangeness asymmetry at the initial Q_0 scale and of using the lattice data for the strangeness asymmetry by comparing the experimental data and theory predictions for ATLAS 7 TeV W and Z differential cross sections as functions of dilepton pseudorapidity [12] (ID=248), dimuon production from (anti)neutrino-DIS process by NuTeV [10] (ID = 124–125) and CCFR [11] (ID=126–127), F_3 structure function measurements by CDHSW [41] (ID = 109) and CCFR [42] (ID=111), E866 NuSea $Q^3 d^2\sigma_{pp}/(dQdx_F)$ [43] (ID=204), and E906 SeaQuest [44] (ID = 206) experiments.

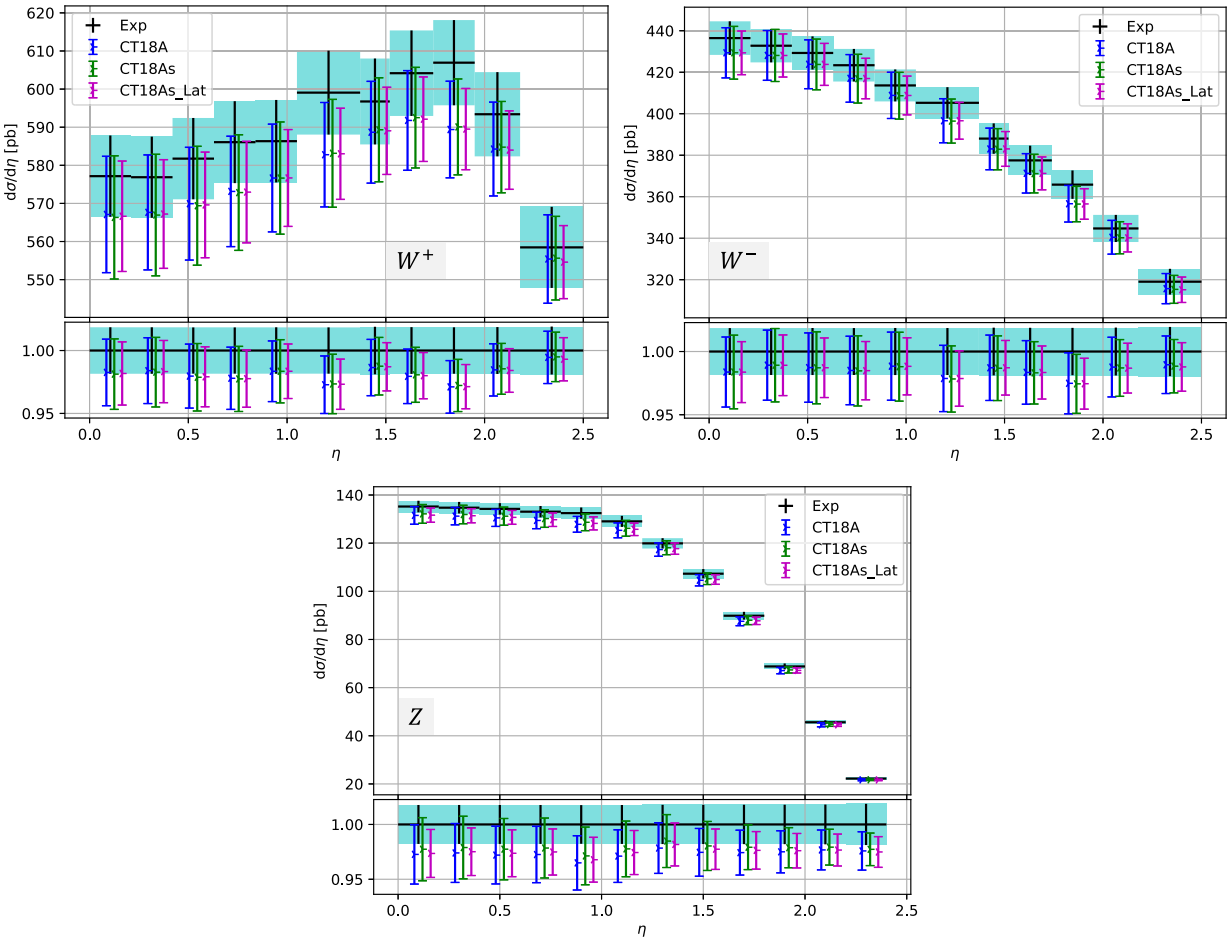

FIG. 6. Comparison of CT18A, CT18As, and CT18As_Lat predictions to the experimental values of ID = 248 ATLAS 7 TeV W and Z differential cross sections for W^+ (top left), W^- (top right), Z (bottom) as functions of dilepton pseudorapidity [12].

TABLE IV. The reduced χ^2 for Z and $W^{\pm}$ production and the contribution of the nuisance parameter (R^2) to the total χ^2 for the ATLAS 7 TeV W and Z data (ID = 248). The reduced χ^2 quantifies the quality of fit to the shifted data. ATLAS 7 TeV W and Z data [12] (ID = 248) contains 131 correlated systematic errors.

	Z	W^+	W^-	R^2 ($R^2/131$)	Reduced χ^2	Total χ^2
CT18A	17.48	15.29	13.82	40.99 (0.31)	46.59	87.58
CT18As	15.78	15.72	11.96	32.13 (0.25)	43.46	75.59
CT18As_Lat	17.22	14.58	12.94	34.36 (0.26)	44.74	79.10
N_{pt}	12	11	11		34	34

A. ATLAS 7 TeV W and Z production at the LHC

As discussed in Appendix F. 2 of Ref. [1], the large increase in the contribution of the nuisance parameters, associated with the correlated systematic errors of the ATLAS 7 TeV W and Z production data [12] (ID = 248), to its total χ^2 value after ePump updating [57,58] indicates the presence of some tensions with NuTeV [10] and CCFR [11] DIS dimuon data. Similar discussions regarding the systematic uncertainty correlations of the ATLAS 7 TeV W and Z data were also presented in Refs. [2,3,7]. In Fig. 6, we compare the unshifted ATLAS 7 TeV W and Z data to the theoretical predictions of CT18A, CT18As, and CT18As_Lat. The central values of the predictions for all the W and Z data are below the experimental measurements and on the edge or even outside of the experimental error bands. However, considering PDF-induced uncertainties, all predictions are consistent with the experimental

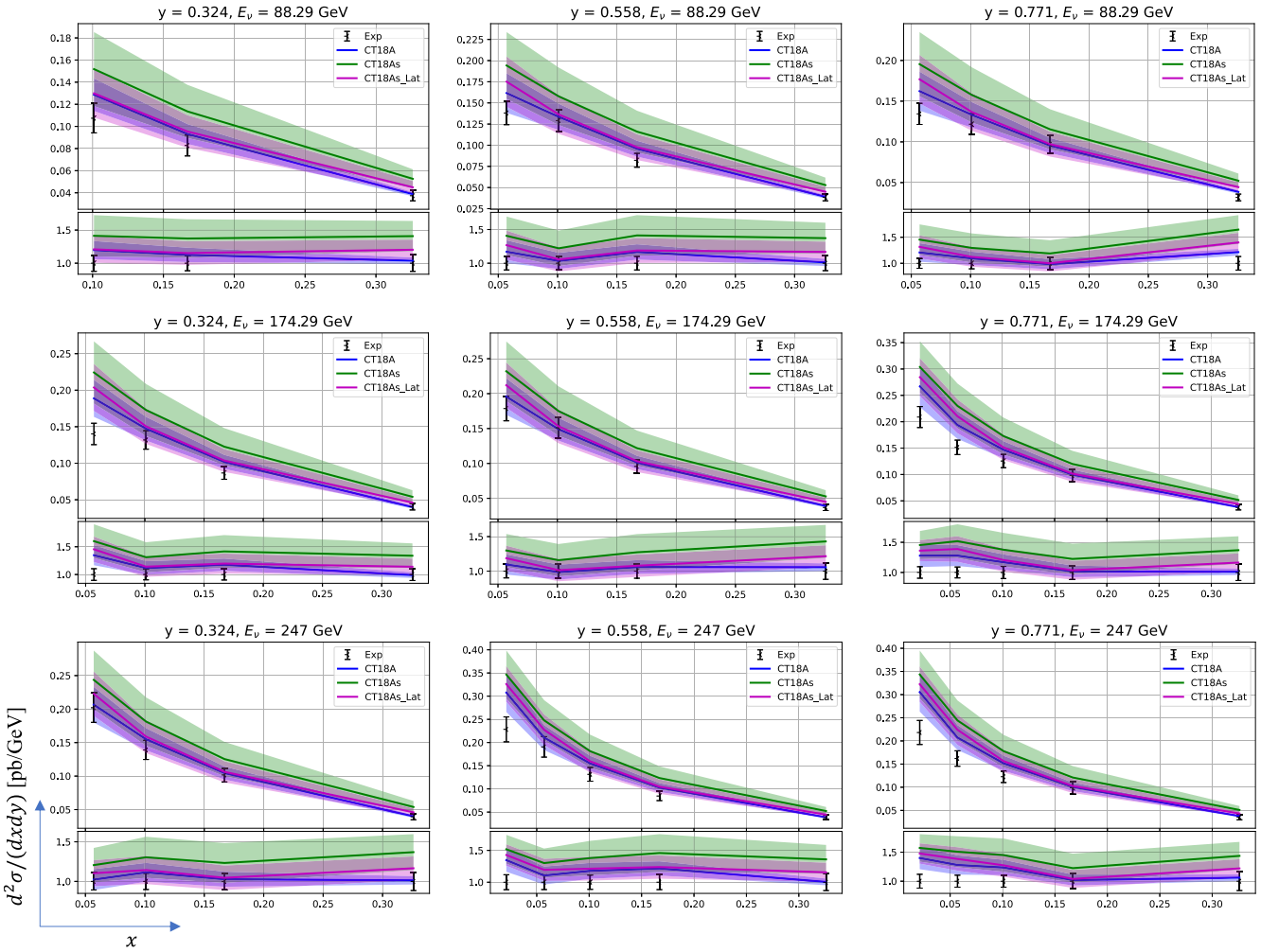

FIG. 7. Comparison of data and theories for NuTeV measurements of dimuon production [10] in neutrino-ion collisions (ID = 124). The unshifted data is presented in the form of $d^2\sigma/dxdy$ [pb/GeV] as a function of x for a certain values of y and the neutrino energy E_ν.

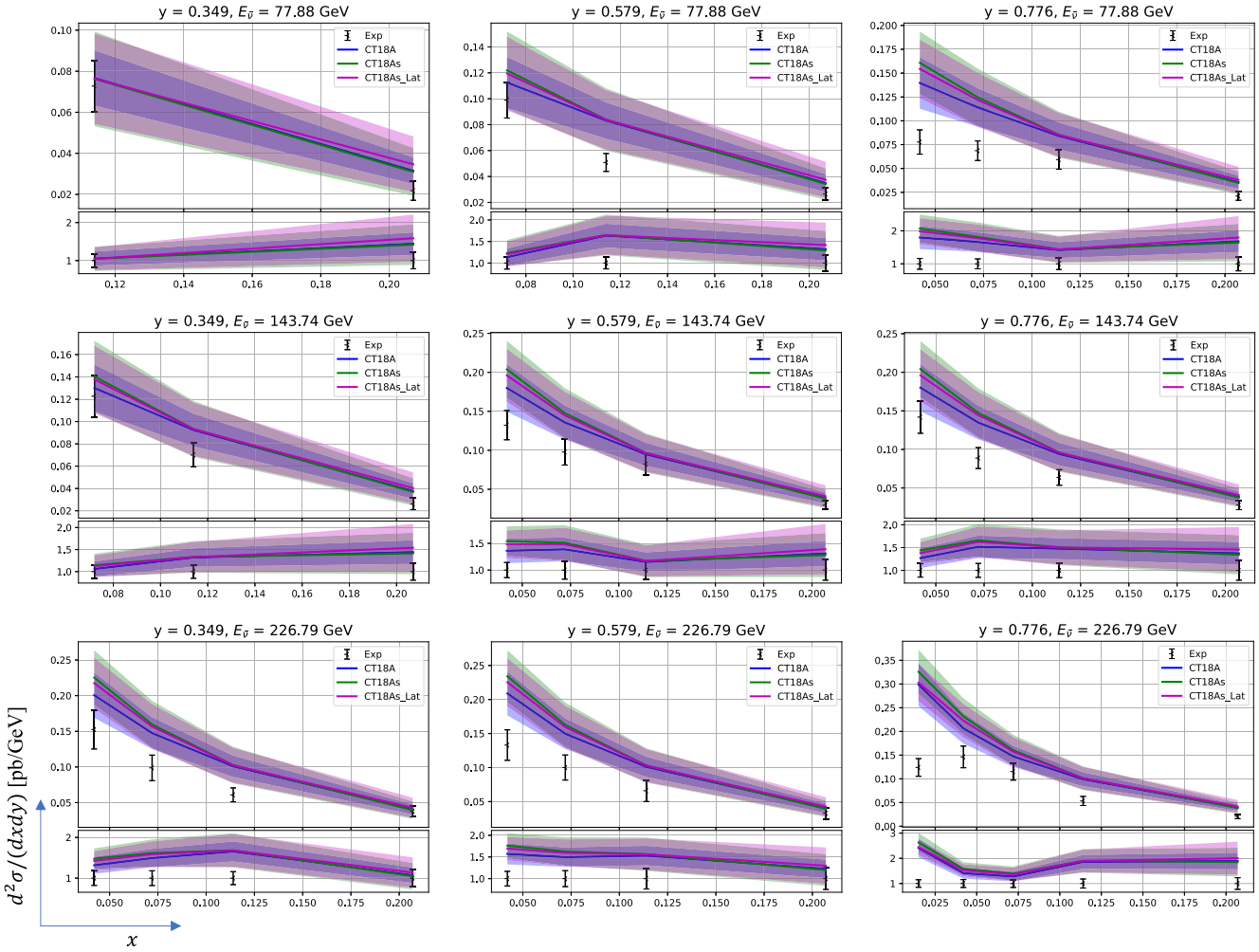

FIG. 8. Similar to Fig. 7, but in antineutrino-ion collisions (ID = 125).

measurements. The differences among the predictions of CT18A, CT18As, and CT18As_Lat for $W^{\pm}$ production (top panels of Fig. 6) are small, compared to the large uncertainty. In Table IV, by allowing a nonvanishing strangeness asymmetry at Q_0 scale, the reduced χ^2 for the W^- production data is improved, while it is almost unchanged for the W^+ production data. The improvement relative to the W^- production (via $s\bar{u}, s\bar{c} \to W^-$) data can be understood from Fig. 4, where $s(x)$ is enhanced with a nonvanishing strangeness asymmetry, while $\bar{s}(x)$ is less affected. In CT PDF global analysis [40,59], the χ^2 of a certain experimental measurement receives contributions from two parts, $\chi^2 = \chi^2_{\text{red}} + R^2$. The term R^2 is the sum of the square of nuisance parameters associated with each of the correlated systematic uncertainties, and it is analytically minimized with respect to the current optimal PDF. The other part, referred as the reduced chi-square, χ^2_{red}, quantifies the difference between theory prediction and shifted data, in units of the total uncorrelated uncertainty, including both statistical and uncorrelated systematic errors, of every data point.

As for the Z-boson production (bottom panel of Fig. 6), the CT18As prediction is slightly larger than CT18A. Since the production of Z-bosons via the Drell-Yan process is dominated by quark-antiquark fusion, the enhancement in the Z production rate reflects a higher magnitude in the combination of quark and antiquark PDFs. This can be seen in Fig. 4, which shows the total strangeness $s_+(x)$ receiving a higher magnitude if nonzero strangeness asymmetry $s_-(x)$ is allowed. Relative to CT18As, the CT18As_Lat prediction is shifted such that it becomes closer to that of CT18A. Meanwhile, the predicted uncertainty of CT18As_Lat shrinks compared to CT18As.

B. SIDIS dimuon production data

The SIDIS dimuon production data selected for our PDF fits comprises NuTeV [10] and CCFR [11] experiments (ID = 124–127). At leading order, these data sets directly probe $s(x)$ and $\bar{s}(x)$, so they play an important role in determining strange quark and antiquark PDFs. In Figs. 7 and 8, the comparison of the unshifted data of

TABLE V. The reduced χ^2 and the contribution of the nuisance parameter (R^2) to the total χ^2 for the NuTeV measurements of dimuon production in neutrino-ion (ID = 124, $N_{\rm pt} = 38$) and antineutrino-ion (ID = 125, $N_{\rm pt} = 33$) collisions [10]. The NuTeV dimuon production data sets have only one systematic error, which is the normalization error (10%).

	NuTeV ($\nu\mu^+\mu^-$) SIDIS			NuTeV ($\bar{\nu}\mu^+\mu^-$) SIDIS		
	Reduced χ^2	R^2	Total χ^2	Reduced χ^2	R^2	Total χ^2
CT18A	30.43	1.47	31.90	42.20	10.59	52.79
CT18As	21.83	7.44	29.27	48.23	13.27	61.50
CT18As_Lat	33.22	3.08	36.30	40.01	12.75	52.76

the NuTeV measurements of SIDIS dimuon production in neutrino-ion (ID = 124) and antineutrino-ion (ID = 125) collisions [10] to the differential cross-sections, predicted with CT18A, CT18As, and CT18As_Lat PDFs, is presented. The reduced χ^2 and the nuisance parameter contribution (R^2) to the total χ^2 for the NuTeV dimuon data are summarized in Table V. The similar comparison for the CCFR measurements of dimuon production are shown in Figs. 9 and 10, and Table VI.

In Fig. 7, the central values of CT18As predictions for the NuTeV measurement with neutrino beam (ID = 124), which directly probes $s(x)$ at leading order, are found to be so enhanced that they are outside of the experimental uncertainties and deviate from central values of CT18A. Table V shows that the CT18A and CT18As have a

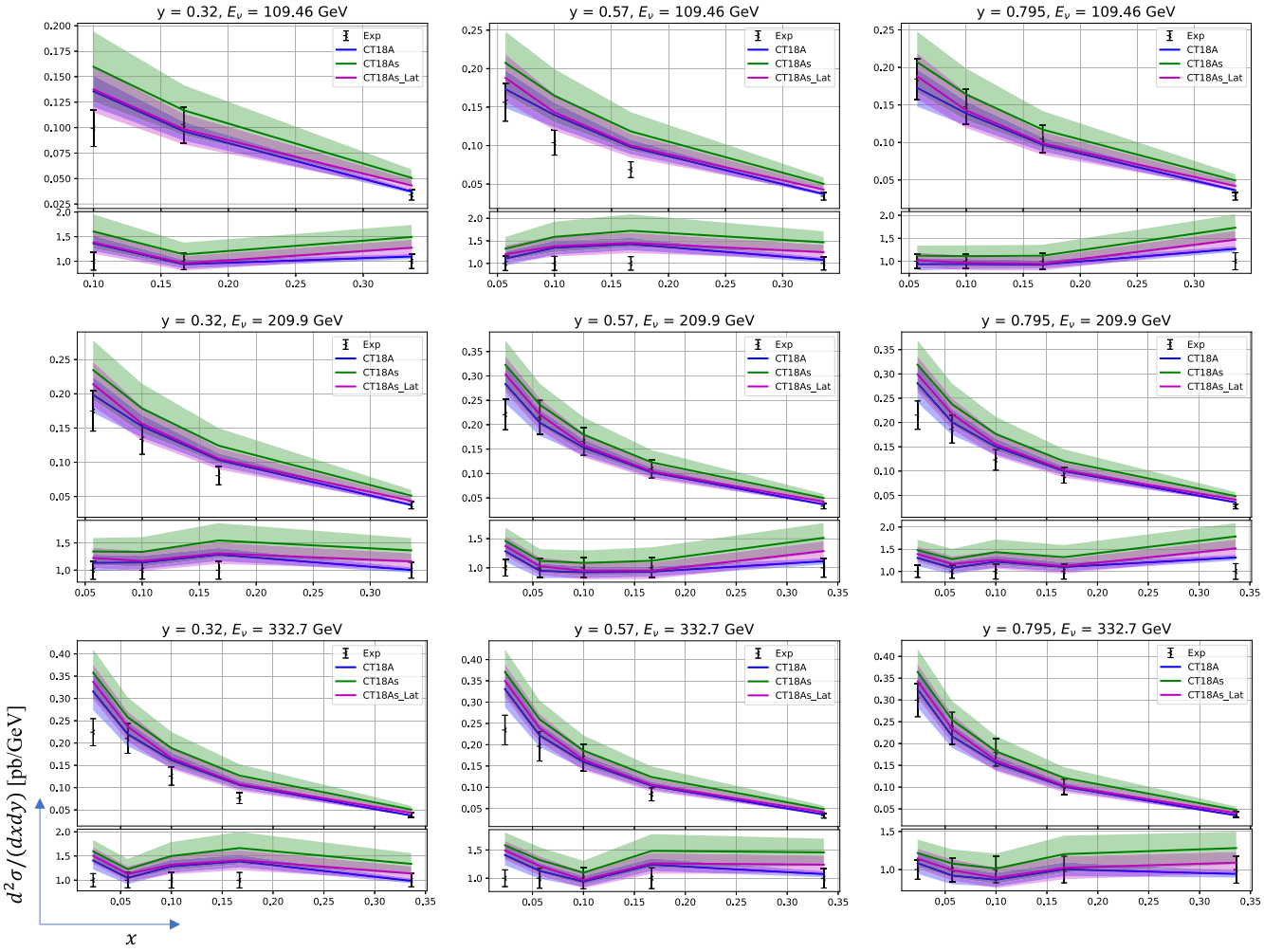

FIG. 9. Comparison of unshifted data and theories for CCFR measurements of dimuon production [11] in neutrino-ion collisions (ID = 126). The data is presented in the form of $d^2\sigma/dxdy$ [pb/GeV] as a function of x for a certain values of y and the neutrino energy E_ν.

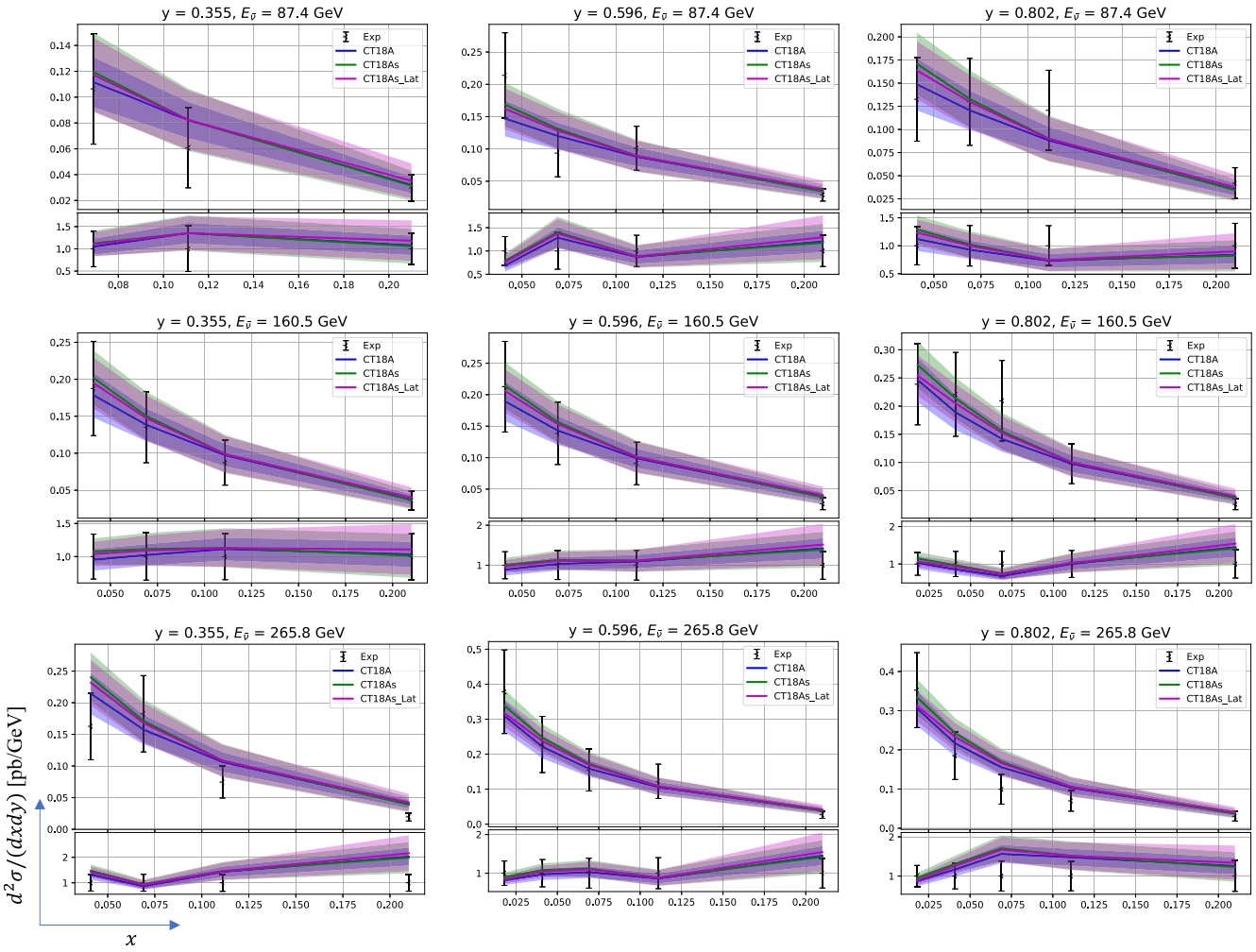

FIG. 10. Similar to Fig. 9, but in antineutrino-ion collisions (ID = 127).

comparable total χ^2 value, but the CT18As can fit the shifted data better with a larger R^2. The tight constraint on strangeness asymmetry $s_-(x)$ of the LQCD calculation strongly impacts the strange PDF, as seen in Fig. 4. Consequently, the prediction of CT18As_Lat in Fig. 7 and the reduced χ^2 shown in Table V are closer to those of CT18A. The uncertainty of CT18As_Lat prediction is then reduced from the wide error band of CT18As prediction, but is still larger than the uncertainty of CT18A prediction. A similar comparison is presented for the NuTeV measurement with antineutrino beam (ID = 125) in Fig. 8. The central values for predictions of all three PDFs are close to each other, though with a much larger $\chi^2/N_{\rm pt}$, about 1.6–1.9, in comparison to that (less than 1) found in the NuTeV measurement with neutrino beam (ID = 124), cf. Table V. In terms of PDF-induced uncertainty in predictions, CT18A has a smaller uncertainty band when compared to CT18As and CT18As_Lat, in which a nonvanishing strangeness asymmetry $s_-(x)$ is allowed at the initial Q_0 scale.

TABLE VI. Similar to Table V. The reduced χ^2 and the contribution of the nuisance parameter (R^2) to the total χ^2 for the CCFR measurements of dimuon production in neutrino-ion (ID = 126, $N_{\rm pt}$ = 40) and antineutrino-ion (ID = 127, $N_{\rm pt}$ = 38) collisions [11]. The CCFR dimuon production data sets have only one systematic error, which is the normalization error (10%).

	CCFR ($\nu\mu^+\mu^-$) SIDIS			CCFR ($\bar{\nu}\mu^+\mu^-$) SIDIS		
	Reduced χ^2	R^2	Total χ^2	Reduced χ^2	R^2	Total χ^2
CT18A	34.04	1.57	35.61	19.69	1.19	20.88
CT18As	33.08	7.66	40.74	16.56	1.95	18.51
CT18As_Lat	32.65	3.34	35.99	20.11	2.27	22.38

We show the comparisons of data and theory for the CCFR dimuon production [11] in Figs. 9 and 10. The reduced χ^2 and the nuisance parameter contribution (R^2) for the CCFR dimuon data are summarized in Table VI. We observed the similar phenomena as in CCFR measurements as those seen in the NuTeV dimuon production [10] with neutrino beam (ID = 124). The χ^2 for the CCFR dimuon data with neutrino beam (ID = 126) is slightly increased in CT18As by a large shift to the data. With the inclusion of the lattice data, the CT18As_Lat obtain a comparable fit quality with the CT18A. Unlike the fits to the NuTeV dimuon data with antineutrino beam (ID = 125), all three PDFs can fit the CCFR dimuon data with antineutrino beam (ID = 127) well.

As shown in Tables II, V, and VI, the descriptions to both NuTeV and CCFR dimuon data are in general good, except the NuTeV dimuon data with antineutrino beam (ID = 125). For both NuTeV and CCFR dimuon data, a large shift to the raw data, hence a large R^2 penalty, is required to fit the shifted data. In terms of the total χ^2, no

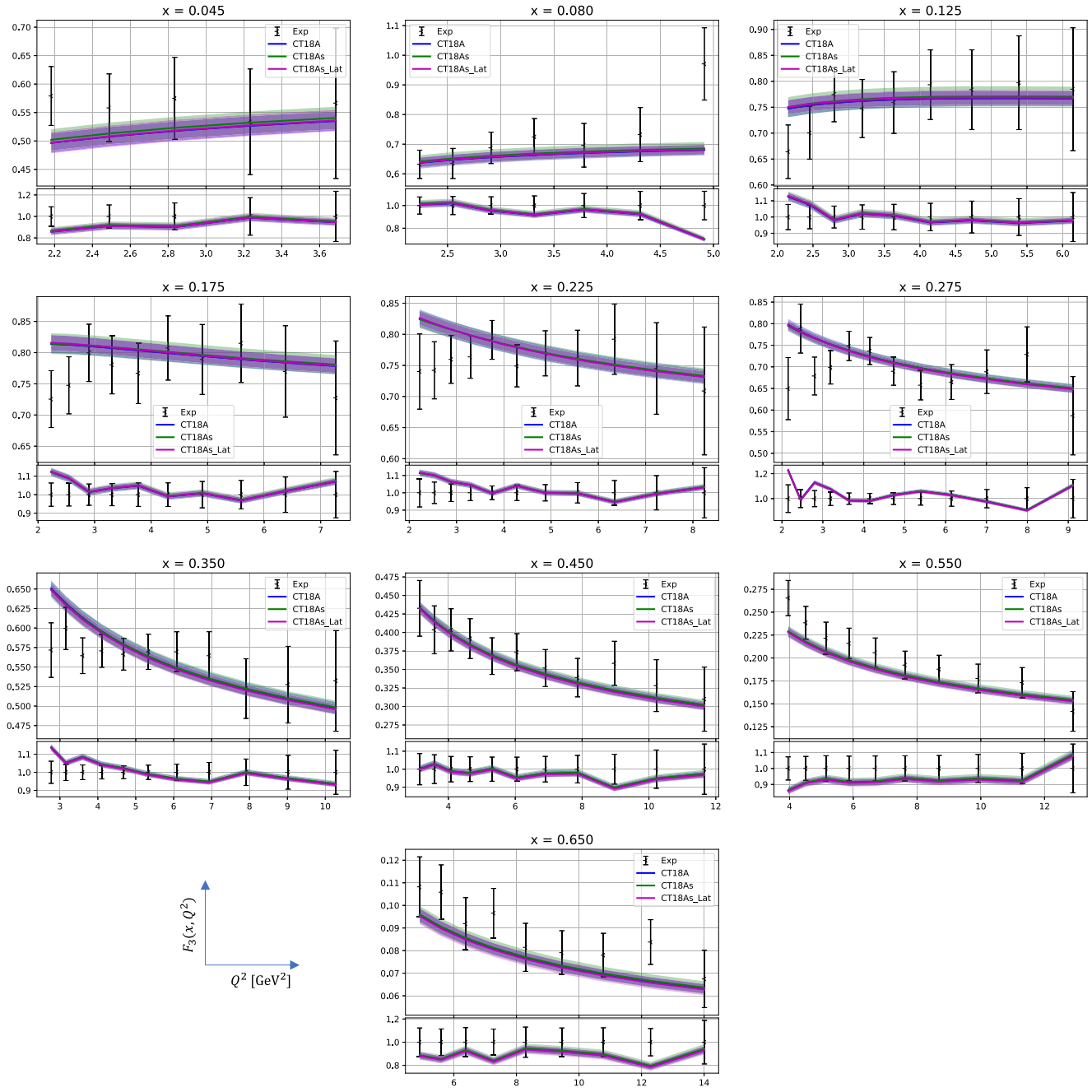

FIG. 11. Comparison of data and theories for the CDHSW F_3^p structure function measurements [41] (ID = 109). The unshifted data are presented in the form of F_3 as a function of Q^2 for a certain values of x.

significant improvement is observed for the NuTeV and CCFR dimuon data altogether, if a nonvanishing strangeness asymmetry $s_-(x, Q_0)$ is allowed. Further, introducing the LQCD calculation of the strangeness asymmetry $s_-(x)$ in the CT18As_Lat results in comparable descriptions of these data sets to the CT18A. Though, as been seen in Sec. IV A, improvements for the R^2 penalty, reduced χ^2, and hence the total χ^2 for ATLAS 7 TeV W and Z data [12] (ID = 248) are found in the CT18As, we did not find a clear evidence that allowing a nonvanishing strangeness asymmetry in the CT18As fit could release the above mentioned tension it is better to specify the tension here, as compared to the CT18A fit.

Before closing this subsection, we would like to give a final comment about the large R^2 values observed in the above discussion. In the CT analyses, the CCFR and NuTeV dimuon cross sections are calculated by assuming the $c \to \mu$ branching ratio of 0.099, as in Sec. 5.2.1 of [10]. The normalization uncertainty of 10% is treated as fully correlated over the ν channel and similarly over the $\bar{\nu}$ channel. In this work, we confirmed the finding in Ref. [1] that reducing the $c \to \mu$ branching ratio from 0.099 to 0.092, as adopted by MMHT [60], only marginally increases $s(x, Q)$ in CT18 at $x > 0.1$, while slightly reducing the CCFR and NuTeV χ^2 values in the CT18A fit. Roughly, this will reduce the R^2 values of the NuTeV and CCFR SIDIS dimuon data listed in Tables V and VI, by about one to two units, with a much smaller effect on their reduced χ^2. Similar reduction (by about one to two units) in the total χ^2 value of ATLAS 7 TeV W and Z data is also observed.

C. F_3 structure function

The F_3 structure function at leading order is proportional to the valence-sector PDFs, so it is sensitive to the strangeness asymmetry $s_-(x)$. Since $u_-(x)$ and $d_-(x)$ PDFs already receive tight constraints from many other data sets included in the fit, it is expected that the variation in predictions of the F_3 structure function should reflect

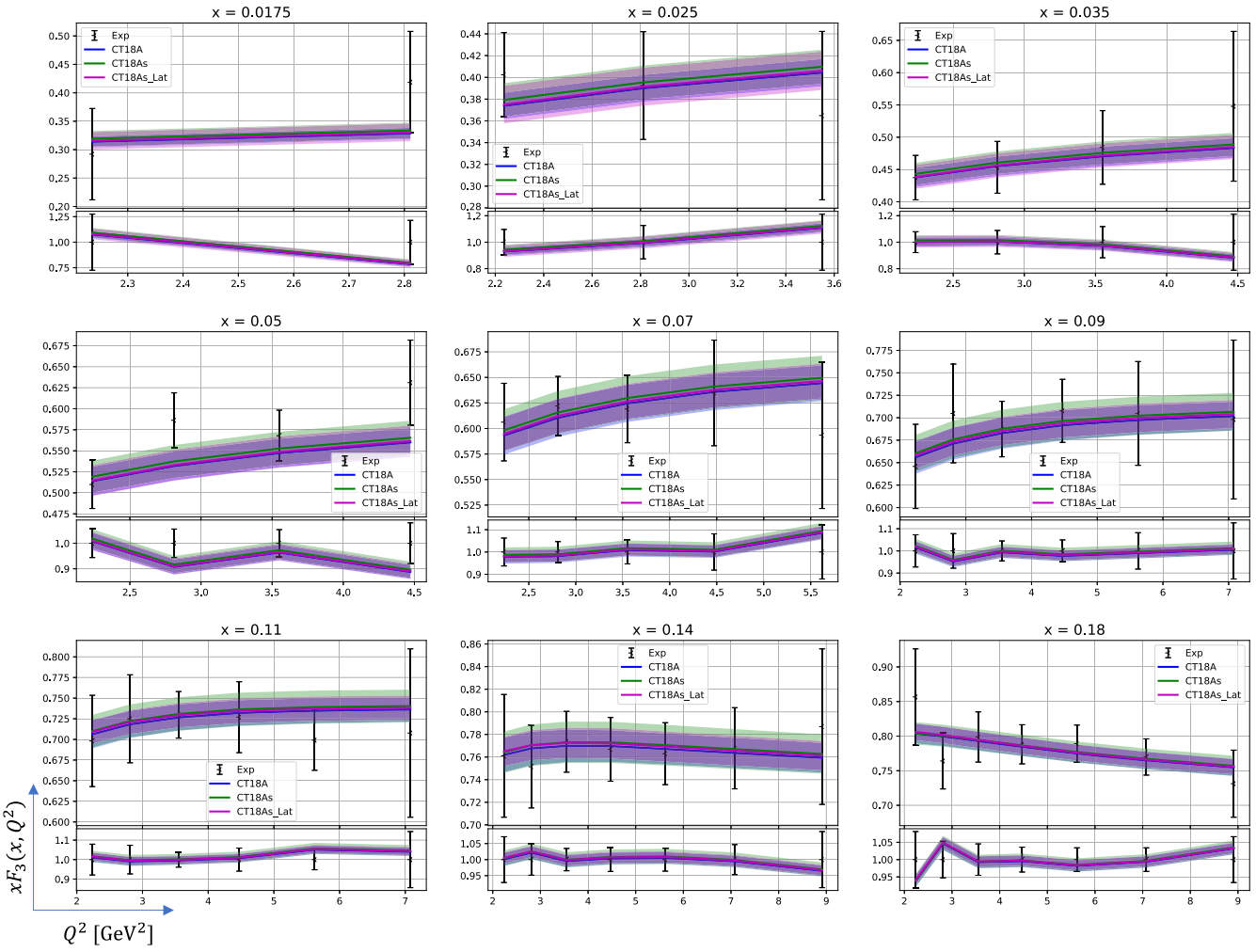

FIG. 12. Comparison of data and theories for the CCFR xF_3^p structure function measurements [42] (ID = 111). The unshifted data are presented in the form of xF_3 as a function of Q^2 for a certain values of x. Larger values of x are shown in Fig. 13 below.

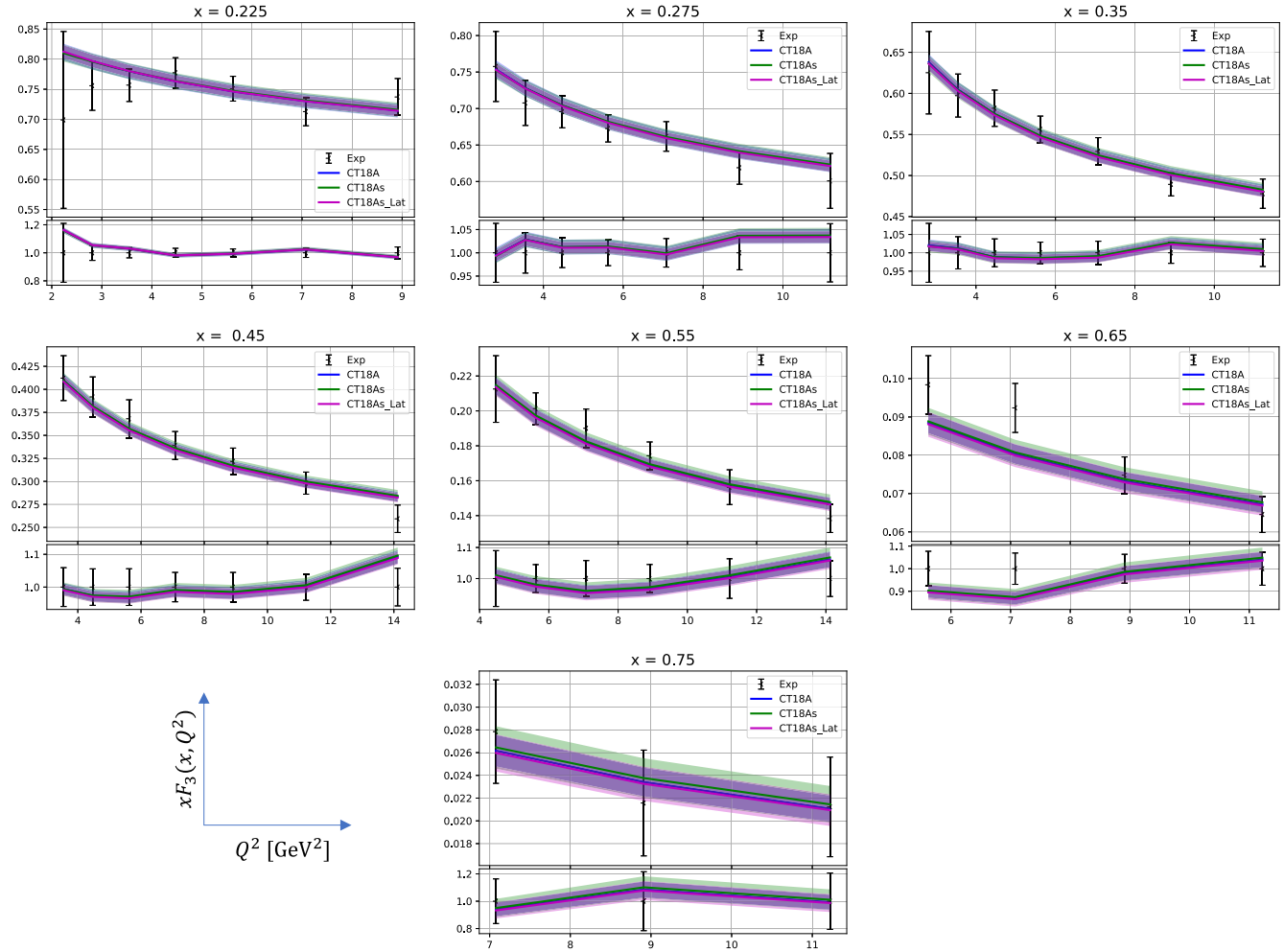

FIG. 13. Following Fig. 12, the comparison of data and theories for CCFR xF_3^p structure function measurements [42] (ID = 111) for larger x.

the information in the $s_-(x)$ distribution. The CERN-Dortmund-Heidelberg-Saclay-Warsaw (CDHSW) F_3^p structure function measurement [41] (ID = 109) and CCFR xF_3^p structure function measurement [42] (ID = 111) are two F_3-measurement data sets included in CT18A, CT18As, and CT18As_Lat. In Figs. 11–13, we study the implications of the $s_-(x)$ distribution in the comparison of data and theory for the CDHSW and CCFR F_3 measurements.

We show that the predictions of CT18A, CT18As, and CT18As_Lat for the CDHSW F_3^p structure function are consistent with experiment in Fig. 11. For $x \leq 0.125$ and $x \geq 0.35$, the central values of the predictions of CT18As have a slightly higher magnitude than those of CT18A and CT18As_Lat, in which less strangeness asymmetry is predicted. But for x around 0.1–0.2, where the predicted strangeness asymmetry in CT18As peaks, the difference among predictions of the three PDFs is not obvious. This is because the F_3 prediction also receives contributions from $u_-(x)$ and $d_-(x)$, whose magnitudes are much greater than the strangeness asymmetry $s_-(x)$. For x around 0.1–0.2, the predicted uncertainty of CT18As is larger than those of CT18A and CT18As_Lat. In this range of x, CT18As has the largest uncertainty for the strangeness asymmetry $s_-(x)$, cf. Fig. 4. In Figs. 12 and 13, a similar comparison of data and theory is done for the CCFR xF_3^p structure function measurement. An upward shift of the central value and an enlarged uncertainty in the CT18As prediction are also observed for this case.

D. E866 NuSea data and E906 SeaQuest data

In Fig. 2, we find that the fixed-target E866 NuSea $Q^3 d^2\sigma_{pp}/(dQdx_F)$ data [43] (ID = 204) has effective Gaussian variables $S_E > 2$, suggesting that this data cannot be well fitted. In Figs. 14 and 15, the E866 NuSea data is compared to theoretical predictions of CT18A, CT18As, and CT18As_Lat. We observe that, for $0.17 < x_F < 0.73$, there is a trend that central values of numerical predictions are above the experimental data points. The difference

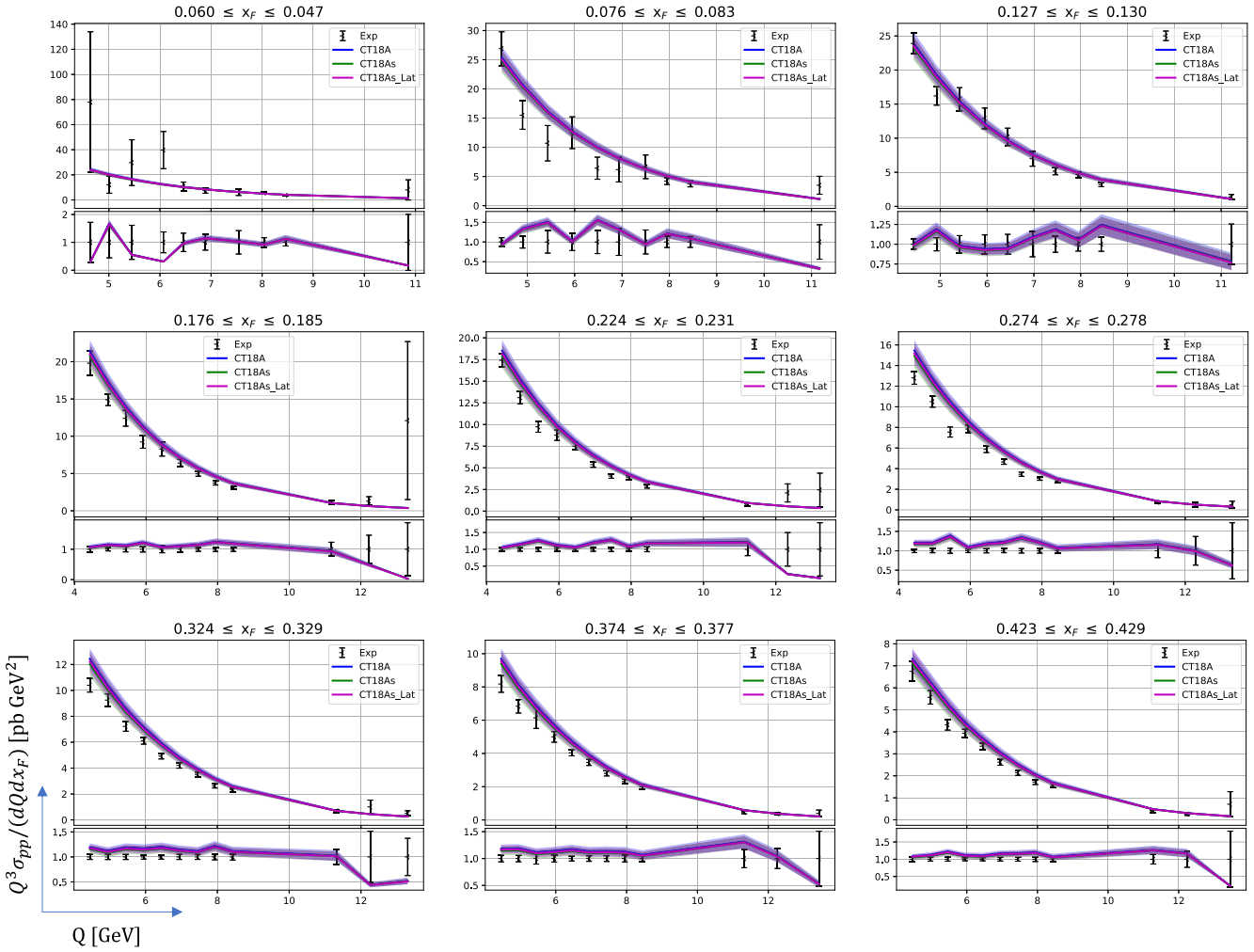

FIG. 14. Comparison of data and theories for the E866 NuSea measurement of $Q^3 d^2\sigma_{pp}/(dQdx_F)$ [43] (ID = 204). The unshifted data is presented in the form of $Q^3 d^2\sigma_{pp}/(dQdx_F)$ as a function of invariant mass Q for ranges of x_F. Larger values of x_F are shown in Fig. 15.

among theoretical predictions is only noticeable for bins with $x_F > 0.6$. Allowing a nonzero strangeness asymmetry at the initial Q_0 scale pulls theory predictions downward, and hence produces a slightly better fit to E866 NuSea $Q^3 d^2\sigma_{pp}/(dQdx_F)$ data. The χ^2 value decreases from CT18A to CT18As, as observed in Table II. Figure 5 shows that allowing a nonvanishing strangeness asymmetry at Q_0 scale would enhance the total strangeness, whose cost is the suppression on $\bar{u}$ and $\bar{d}$ for $0.01 < x < 0.1$, due to the conservation of the total momentum sum rule. Considering that $u(x)$ and $d(x)$ in large-x region would be less affected by variation in the strangeness asymmetry $s_-(x)$, the decreases in $\bar{u}(x)$ and $\bar{d}$ leads to less numerical value of production cross-section $Q^3 d^2\sigma_{pp}/(dQdx_F)$ prediction.

Below, we compare in detail the quality of various fits to the E866 NuSea [61] $\sigma(pd)/2\sigma(pp)$ data (ID = 203), and the predictions of those PDF sets to the E906 SeaQuest [44] data (ID = 206). We note that the E906 SeaQuest data is not included in the CT18A data set, neither in this study. Both E866 NuSea (ID = 203) and E906 SeaQuest (ID = 206) data measure the ratio of cross sections $\sigma(pd)/2\sigma(pp)$, as a function of the momentum fraction x_2 of the target. This ratio approximates the ratio of antiquark PDFs, for $\sigma(pd)/2\sigma(pp) \approx (1+\bar{d}_p(x_2)/\bar{u}_p(x_2))/2$ in the kinematic region probed by these data sets. Thus, these data sets provide useful information on antiquark PDF asymmetry in the large-x region.

As shown in Fig. 2, the effective Gaussian variables of these two data sets for all three PDFs are close to zero, indicating that all three PDFs describe both the NuSea and SeaQuest data well, as shown by chi-squares in Table VII. In Fig. 16 we compare theory predictions of CT18A, CT18As, and CT18As_Lat to the E906 SeaQuest data, and find that they are all consistent with experimental values. From predictions of CT18A to CT18As,

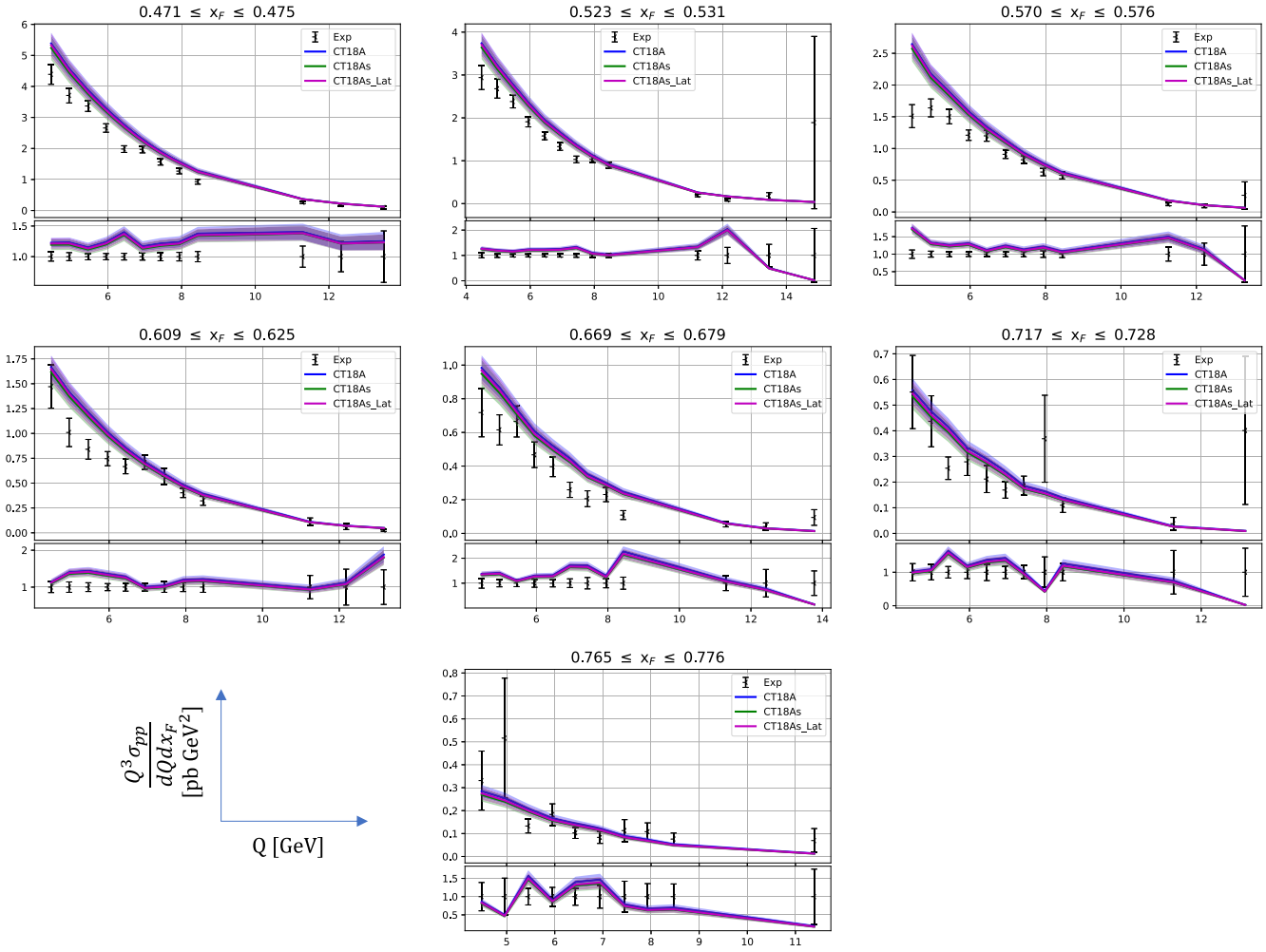

FIG. 15. Following Fig. 14, the comparison of the unshifted data and theories for E866 NuSea $Q^3 d^2\sigma_{pp}/(dQdx_F)$ measurement [43] (ID = 204) for larger values of x_F.

introducing the strangeness asymmetry at the initial Q_0 scale would raise the central values, so becoming more consistent with the E906 SeaQuest data. As shown in the bottom panel of Fig. 5, allowing a nonvanishing strangeness asymmetry at Q_0 scale in CT18As leads to an increased PDF ratio $\bar{d}/\bar{u}(x)$ for $x > 0.2$, which is favoured by the E906 SeaQuest data. It is known [62], and shown in Figs. 16 and 17, that the E906 SeaQuest data seem to prefer an opposite trend of $\bar{d}/\bar{u}(x)$ in the large-x region, as compared to its predecessor, the E866 NuSea (ID = 203) measurement. However this tension is not evident in Fig. 2 and Table VII. The introduction of a nonvanishing strangeness asymmetry at Q_0 scale slightly changes the prediction of the E866 NuSea data (ID = 203), particularly for the last two bins with the highest values of x_2 in Fig. 17, where predictions of the CT18As are pulled away from the E866 NuSea (ID = 203) data points. The reason for the weakened fit to these bins is same as the reason for the improvement of the CT18As fit to the E906 SeaQuest data (ID = 206). But all three PDFs still well fit the E866 NuSea data (ID = 203) in overall, as the weakened fit to bins with high x_2 trading off with the

TABLE VII. Similar to Table II, but for the E866 NuSea data [61] (ID = 203) and E906 SeaQuest data [44] (ID = 206) only. Note that the E906 SeaQuest data was not included in any of the PDF fits performed in this study, and its χ^2 values were calculated by using the corresponding PDFs.

ID	Experimental data set	$N_{\mathrm{pt},E}$	CT18A	CT18As	CT18As_Lat
203	E866 Drell-Yan process $\sigma_{pd}/(2\sigma_{pp})$ [61]	15	17.6	17.6	17.4
206	E906 Drell-Yan process $\sigma_{pd}/(2\sigma_{pp})$ [44]	6	5.5	4.5	5.0

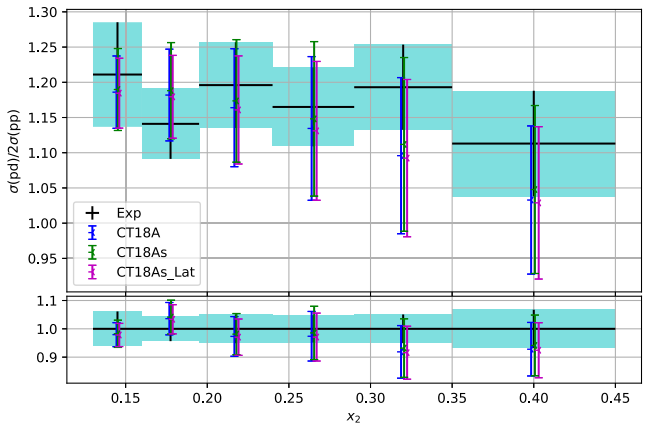

FIG. 16. Comparison of the unshifted data and theories for E906 SeaQuest data [61] (ID = 206). We note that this data is not included in PDF fits for this study, and other fits of the CT18 PDF family.

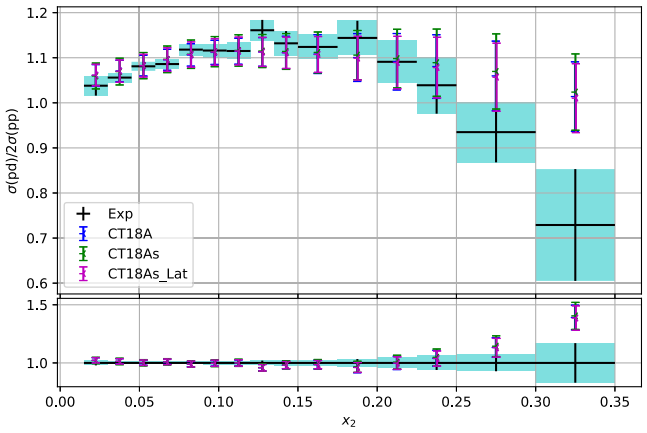

FIG. 17. Comparison of the results of various fits and the unshifted data of the E866 NuSea measurement of $\sigma_{pd}/(2\sigma_{pp})$ [61] (ID = 203).

improved fit to other bins. The changes of the effective Gaussian variable in Fig. 2 and of the χ^2 in Table VII for this data are negligible. Hence, allowing a nonvanishing strangeness asymmetry at the initial scale under the framework of the CT18A fit cannot provide a decisive discrimination on the known tension between the E866 NuSea [61] and the E906 SeaQuest [44] data. Furthermore, the last column of Table VII indicates that the inclusion of the lattice data in the CT18As_Lat fit results in a somewhat reduced χ^2 value for the NuSea data, and an increased one for the SeaQuest data, as compared to the CT18As predictions.

V. CONCLUSION AND OUTLOOK

In this work we study the impact of the lattice data on the determination of the strangeness asymmetry distribution $s_-(x) \equiv s(x) - \bar{s}(x)$ at the initial Q_0 scale in the general CTEQ-TEA global analysis of parton distribution functions of the proton. Following the recommendation made in Ref. [1], we start with the CT18A NNLO fit, rather than the nominal CT18 NNLO fit, because we are interested in the (anti)strange quark distributions of the proton. The ATLAS $\sqrt{s} = 7$ TeV W, Z combined cross section data [12] (ID = 248) is included in the CT18A fit, while it is absent in the nominal CT18 fit.

We extend the nonperturbative parametrization in the CT18A analysis by allowing a strangeness asymmetry distribution $s_-(x) \equiv s(x) - \bar{s}(x)$ at the initial Q_0 (= 1.3 GeV) scale. The resulting PDF set from the CT18A data set is labeled as CT18As, whose quality of fit is similar to that of the CT18A fit. The constraint from the lattice data into the PDF global fit is added by using the Lagrange multiplier method. We found that the resulting PDF, named as CT18As_Lat, present a different strangeness asymmetry distribution and a smaller uncertainty band than those of CT18As. We also investigate the possible constraint of the lattice data with higher precision by performing a PDF fit with errors in the original lattice data points reduced by half. Our results conclude that the current lattice data is able to help further constraining the strangeness asymmetry $s_-(x)$ in PDF global analysis. Future precision improvement in the lattice calculation of this quantity could further improve the $s_-(x)$ for $x \in [10^{-2}, 0.6]$.

We also assess the impact of introducing a nonvanishing strangeness asymmetry $s_-(x)$ at the initial Q_0 scale and lattice data by comparing predictions of CT18A, CT18As, and CT18As_Lat on a few selected experimental data. The predictions of different PDFs are in general consistent with each other. As noted in Ref. [1], the CT18A fit reveals tensions between the precision ATLAS $\sqrt{s} = 7$ TeV W, Z data [12] and the NuTeV [10] and CCFR [11] SIDIS dimuon data. In this study, we find that in the CT18As fit, the ATLAS 7 TeV W and Z production data [12] can be better described by an enhanced strange quark distribution $s(x)$, and $s(x) + \bar{s}(x)$, while the improvement in the quality of the fit to the NuTeV and CCFR SIDIS dimuon data is not evident.

Finally, we note that in this work, we have confined ourselves to analyzing the same experimental data set as those included in the CT18A fit, except the specific lattice data on the strangeness asymmetry [25]. To further constrain the s and $\bar{s}$ PDFs in future studies, one may consider, in addition to the SeaQuest data [44], the $W^{\pm}$-boson production associated with charm-quark jets [63–65] at the LHC. The total strangeness PDF distribution can also be constrained by charmed-tagged to inclusive cross section ratios measured by the NOMAD experiment [66].

We make available grids for the CT18As and CT18As_Lat NNLO PDFs described above as a part of

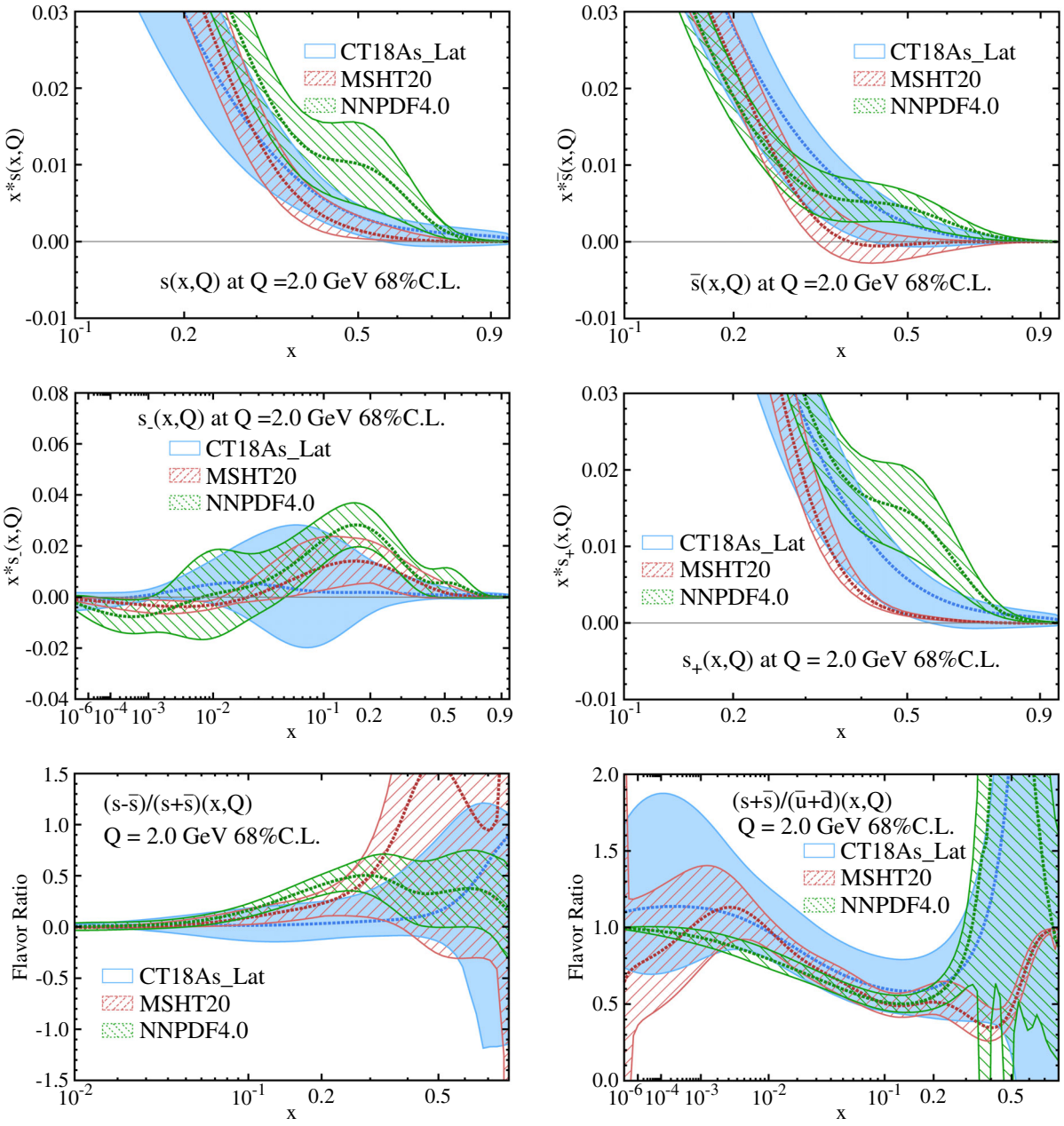

FIG. 18. The comparisons of $s(x)$, $\bar{s}(x)$, $s_-(x)$, $s_+(x)$, $(s+\bar{s})/(\bar{u}+\bar{d})(x)$, and $(s-\bar{s})/(\bar{s}+\bar{s})(x)$ for CT18As_Lat, CT18As2_Lat, MSHT20 [2], and NNPDF4.0 [3] at $Q = 2.0$ GeV.

the LHAPDF library [67] and at the CTEQ-TEA website [68]. The CT18As2_Lat, defined in App. A, is a variant fit similar to the CT18As_Lat, but with an alternative parametrization for strange quark and antiquark PDFs. As to be discussed in Appendix A, the CT18As2 has a moderate PDF ratio $(s+\bar{s})/(\bar{u}+\bar{d})(x)$ in the large-x region, so does the CT18As2_Lat, while CT18As_Lat and CT18As2_Lat PDFs present comparable descriptions to experimental data. A few comparisons of PDF combinations related to strange quark and antiquark PDFs for CT18As_Lat, MSHT20 [2], and NNPDF4.0 [3] are shown in Fig. 18, for reference.

With the release of CT18As and CT18As_Lat, we also update the CT18 PDF series, in the LHAPDF library, with a better numerical precision in providing PDFs for Q crossing the heavy (charm and bottom) parton-mass threshold, and for x approaching to 1. There is no significant difference from the version of CT18 already on LHAPDF.

ACKNOWLEDGMENTS

We thank Rui Zhang for early-state participation in this work and our CTEQ-TEA colleagues for useful discussions. This work is partially supported by the U.S. National

Science Foundation under Grants No. PHY-1653405, No. PHY-2013791 and No. PHY-2209424. H. L. thanks the MILC Collaboration for sharing the lattice configurations. This research used CHROMA software suite [69] and resources of the National Energy Research Scientific Computing Center, a DOE Office of Science User Facility supported by the Office of Science of the U.S. Department of Energy under Contract No. DE-AC02-05CH11231 through ERCAP, facilities of the USQCD Collaboration are funded by the Office of Science of the U.S. Department of Energy, and the Extreme Science and Engineering Discovery Environment (XSEDE) supported by National Science Foundation Grant No. 1548562. The work of H. L. is partially supported by the Research Corporation for Science Advancement through the Cottrell Scholar Award. C. P. Y. is also grateful for the support from the Wu-Ki Tung endowed chair in particle physics.

APPENDIX A: PARAMETRIZATION DEPENDENCE FOR PDF RATIO $(s+\bar{s})/(\bar{u}+\bar{d})(x)$ IN LARGE-x

In Sec. III, we found that the central prediction for the PDF ratio $(s+\bar{s})/(\bar{u}+\bar{d})(x)$ of CT18As and CT18As_Lat for $x > 0.2$ is enhanced comparing to CT18A, as shown in the bottom panel of Fig. 4. This feature is caused by the choice of the more flexible nonperturbative parametrization form of the (anti)strange PDF adopted in the CT18As fit, in comparing to that in CT18. Since the (anti)strange PDF is less constrained by data at such large x values, we examine in this Appendix an alternative fit with an additional theory prior to constrain the ratio of $(s+\bar{s})/(\bar{u}+\bar{d})(x)$ as x approaching to 1. This alternative parametrization enforces strange and antistrange distributions having the same behavior in the large-x limit as up and down quark distributions. The resulting PDF is denoted as "CT18As2". Specifically, it is done as follows. The general functional form, in terms of the free parameters a_k at the initial scale Q_0, is given in Eq. (B1) in the Appendix B and summarized in the Appendix C of the CT18 distributions paper [1]. The coefficients a_1 and a_2, cf. Eq. (B1), control the asymptotic behavior of $f_{(i)}(x, Q_0)$ in the limits $x \to 0$ and 1 respectively. In CT18As, we bind the high-x exponents of the $\bar{u}$, and $\bar{d}$ distributions, $a_2^{\bar{u}} = a_2^{\bar{d}}$, to stabilize $\bar{d}/\bar{u}$ for $x \to 1$, while allowing a_2^s and $a_2^{\bar{s}}$ to be fit independently. However, in CT18As2, we impose a stronger theory prior to bind the high-x exponents of the $\bar{u}$, $\bar{d}$, s and $\bar{s}$ distributions, $a_2^{\bar{u}} = a_2^{\bar{d}} = a_2^s = a_2^{\bar{s}}$, to stabilize both $\bar{d}/\bar{u}$ and $(s+\bar{s})/(\bar{u}+\bar{d})$ for $x \to 1$.

The alternative parametrization impacts mostly in the strange PDF in the large-x region. As shown in in Fig. 19, the strange PDF in CT18As2 for $x > 0.3$, at $Q = 1.3$ GeV, is suppressed as compared to that in CT18As. We note that the apparent negative CT18As2 $\bar{s}$-PDF for x around 0.4 arises from the numerical precision for calculating the PDF error band. In Fig. 20 the strangeness asymmetry $s_-(x)$ in CT18As2 is fairly similar to that in CT18As, except for $x > 0.4$ where the $s_-(x)$ in CT18As2 vanishes, for the strange and antistrange PDFs themselves vanishing fast in this region. The comparisons of PDF ratios $(s-\bar{s})/(s+\bar{s})(x)$ and $(s+\bar{s})/(\bar{u}+\bar{d})(x)$, at $Q_0 = 1.3$ GeV, are respectively displayed in the bottom row panels of Fig. 20. It is evident that CT18As and CT18As2 have different trends in those two PDF ratios as x approaching to 1. Nevertheless, CT18As and CT18As2 provide comparable descriptions to the experimental data analyzed in this work. For the CT18As2, the total χ^2_{tot} is 4362, higher than CT18As by 18 units. For the CT18As2_Lat, the total χ^2_{tot} is 4370, only slightly higher than CT18As_Lat by 8 units. The difference in χ^2_{tot} is much smaller than the tolerance ($\Delta\chi^2 = 100$ for 90% CL) used in the CT18 analysis. Finally, we note that after including the lattice data, the resulting CT18As_Lat and CT18As2_Lat fits lead to similar conclusion.

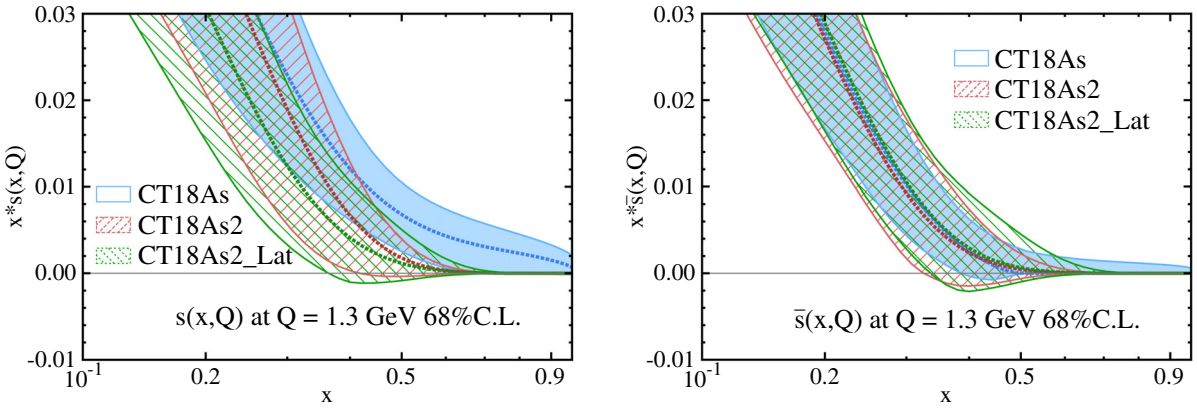

FIG. 19. The comparison of $s(x)$ (left), $\bar{s}(x)$ (right) PDFs at the initial $Q_0(= 1.3\ \text{GeV})$ scale for CT18As, CT18As2, and CT18As2_Lat.

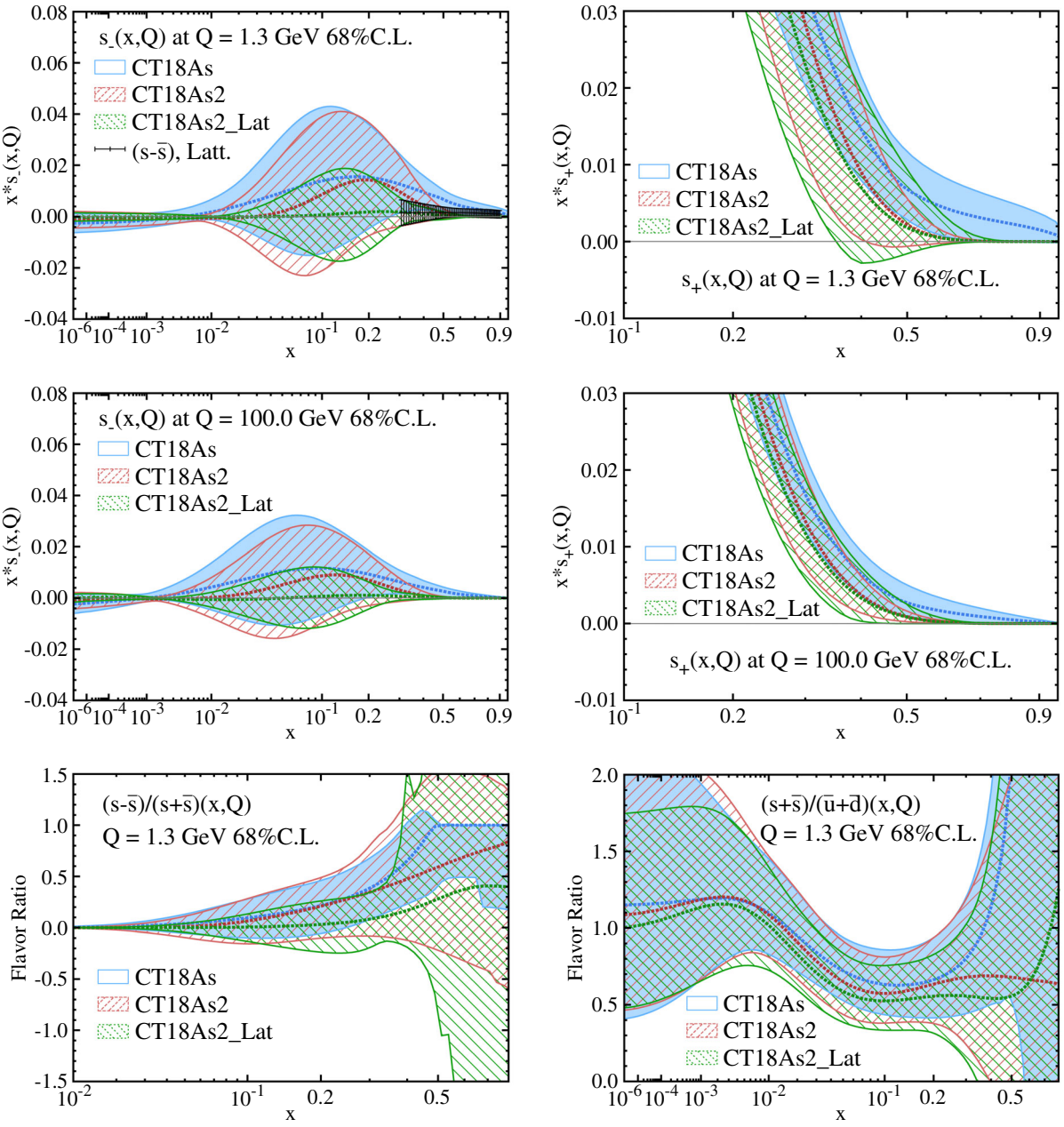

FIG. 20. The comparison of $s_{-}(x)$, and $s_{+}(x)$ PDFs at the initial $Q_0(=1.3\ \mathrm{GeV})$ scale and $Q = 100$ GeV, as well as PDF ratio $(s-\bar{s})/(s+\bar{s})(x)$ and $(s+\bar{s})/(\bar{u}+\bar{d})(x)$ at $Q_0 = 1.3$ GeV, for CT18As, CT18As2, and CT18As2_Lat.

APPENDIX B: NONPERTURBATIVE PARAMETRIZATION FORM OF STRANGENESS

The general CT18 parametrization is reviewed in Appendix C of Ref. [1]. The CT18 parametrization strategy is, out of a wide range of parametric forms at the starting scale $Q_0 = 1.3$ GeV, to find a flexible parametrization, which fits high-energy data without overfitting, and to understand the uncertainties associated to these parameters. In this study, we adopt the CT18 nonperturbative parametrization of u, $\bar{u}$, d, $\bar{d}$, and g PDFs. To obtain fits with nonvanishing strangeness asymmetry of this study, we choose to parametrize $s(x, Q_0)$ and $\bar{s}(x, Q_0)$ PDFs separately, unlike in CT18 parametrization form where $s(x, Q_0) = \bar{s}(x, Q_0)$ is taken. The specific parametrization of $s(x, Q_0)$ and $\bar{s}(x, Q_0)$ for fits in this study is summarized below.

CT PDFs are parametrized with a set of Bernstein polynomials (also called a Bézier curve), such that for the PDF of flavor i,

$$f_{(i)}(x, Q_0) = a_0 x^{a_1-1}(1-x)^{a_2} P_{(i)}(y(a_3, x), a_4, a_5, \ldots) = a_0 \tilde{f}_{(i)}(x, Q_0). \quad \text{(B1)}$$

As stated in Eq. (2), the strangeness asymmetry satisfies the number sum rule, that the net number of strange quarks subtracted by antistrange quark number is zero,

TABLE VIII. Fitted parameter values obtained for the central CT18As_Lat and CT18As2_Lat NNLO fits. The functional forms for each parameterzation are specified in Eqs. (B5) and (B6). (a) Value of a_3 parameter in Eq. (B6) is fixed at 4.0. (b) Values of a_4 and a_5 parameters for $s(x)$ and $\bar{s}(x)$ PDFs are bound together. (c) Values of the denoted parameters for $s(x)$ and $\bar{s}(x)$ PDFs are bound together. (d) Values of the large-x parameter a_2 for both $s(x)$ and $\bar{s}(x)$ distributions are bound with that of $\bar{u}(x)$ and $\bar{u}(x)$.

	CT18As_Lat		CT18As2_Lat	
Central fitted value	$s(x)$	$\bar{s}(x)$	$s(x)$	$\bar{s}(x)$
a_1	$-0.013^{(c)}$	$-0.013^{(c)}$	$-0.021^{(c)}$	$-0.021^{(c)}$
a_2	0.256	3.727	$7.744^{(d)}$	$7.744^{(d)}$
a_3	$4.000^{(a)}$	$4.000^{(a)}$	1.048	1.048
a_4	$0.408^{(b)}$	$0.408^{(b)}$	$-0.059^{(b)}$	$-0.059^{(b)}$
a_5	$0.408^{(b)}$	$0.408^{(b)}$	$-0.059^{(b)}$	$-0.059^{(b)}$
a_6	$0.169^{(c)}$	$0.169^{(c)}$	$1.750^{(c)}$	$1.750^{(c)}$
a_7	0.150	0.228	−1.254	−1.219
a_8	0.004	0.068	2.948	1.530

$$\int_0^1 dx\,(s(x)-\bar{s}(x))=0. \tag{B2}$$

Combining with Eq. (B1), the number sum rule for strangeness asymmetry applies as a constraint on the parametrization form,

$$\int_0^1 dx\,(a_0^{(s)}\tilde{f}_{(s)}(x)-a_0^{(\bar{s})}\tilde{f}_{(\bar{s})}(x))=0. \tag{B3}$$

By given the $a_0^{(\bar{s})}$ fitted value, which is determined as in usual CT18, the overall factor for $s(x,Q_0)$ is found via Eq. (B3),

$$a_0^{(s)}=\frac{\int dx\,a_0^{(\bar{s})}\tilde{f}_{(\bar{s})}(x)}{\int dx\,\tilde{f}_{(s)}(x)}. \tag{B4}$$

The functional form of strangeness distributions is similar to the case in CT18,

$$P(x)=(1-y)^5+a_4 5y(1-y)^4+a_5 10y^2(1-y)^3 + a_6 10y^3(1-y)^2+a_7 5y^4(1-y)+a_8 y^5, \tag{B5}$$

$$y(x)=1-(1-\sqrt{x})^{a_3}. \tag{B6}$$

The best-fit values of $s(x)$ and $\bar{s}(x)$ PDFs parameters for the central PDF of CT18As_Lat and CT18As2_Lat fits are summarized in Table VIII.

[1] T.-J. Hou *et al.*, New CTEQ global analysis of quantum chromodynamics with high-precision data from the LHC, Phys. Rev. D **103**, 014013 (2021).

[2] S. Bailey, T. Cridge, L. A. Harland-Lang, A. D. Martin, and R. S. Thorne, Parton distributions from LHC, HERA, Tevatron and fixed target data: MSHT20 PDFs, Eur. Phys. J. C **81**, 341 (2021).

[3] R. D. Ball *et al.*, The path to proton structure at one-percent accuracy, Eur. Phys. J. C **82**, 428 (2022).

[4] A. Kusina, T. Stavreva, S. Berge, F. I. Olness, I. Schienbein, K. Kovarik, T. Jezo, J. Y. Yu, and K. Park, Strange quark PDFs and implications for Drell-Yan boson production at the LHC, Phys. Rev. D **85**, 094028 (2012).

[5] S. Alekhin, J. Blumlein, L. Caminada, K. Lipka, K. Lohwasser, S. Moch, R. Petti, and R. Placakyte, Determination of strange sea quark distributions from fixed-target and collider data, Phys. Rev. D **91**, 094002 (2015).

[6] S. Alekhin, J. Blümlein, and S. Moch, Strange sea determination from collider data, Phys. Lett. B **777**, 134 (2018).

[7] F. Faura, S. Iranipour, E. R. Nocera, J. Rojo, and M. Ubiali, The strangest proton?, Eur. Phys. J. C **80**, 1168 (2020).

[8] S. Moch, J. A. M. Vermaseren, and A. Vogt, The Three loop splitting functions in QCD: The Nonsinglet case, Nucl. Phys. **B688**, 101 (2004).

[9] S. Catani, D. de Florian, G. Rodrigo, and W. Vogelsang, Perturbative Generation of a Strange-Quark Asymmetry in the Nucleon, Phys. Rev. Lett. **93**, 152003 (2004).

[10] D. A. Mason, Measurement of the strange—antistrange asymmetry at NLO in QCD from NuTeV dimuon data. Ph.D. thesis, Oregon U., 2006.

[11] M. Goncharov *et al.* (NuTeV Collaboration), Precise measurement of dimuon production cross-sections in ν_μ Fe and $\bar{\nu}_\mu$ Fe deep inelastic scattering at the tevatron, Phys. Rev. D **64**, 112006 (2001).

[12] M. Aaboud *et al.* (ATLAS Collaboration), Precision measurement and interpretation of inclusive W^+, W^- and Z/γ^* production cross sections with the ATLAS detector, Eur. Phys. J. C **77**, 367 (2017).

[13] X. Ji, Parton Physics on a Euclidean Lattice, Phys. Rev. Lett. **110**, 262002 (2013).
[14] X. Ji, Parton physics from large-momentum effective field theory, Sci. China Phys. Mech. Astron. **57**, 1407 (2014).
[15] X. Ji, Y.-S. Liu, Y. Liu, J.-H. Zhang, and Y. Zhao, Large-momentum effective theory, Rev. Mod. Phys. **93**, 035005 (2021).
[16] H.-W. Lin, Recent progress on nucleon structure with lattice QCD, Int. J. Mod. Phys. Conf. Ser. **25**, 1460039 (2014).
[17] H.-W. Lin, Calculating the x dependence of hadron parton distribution functions, Proc. Sci., LATTICE2013 (**2014**) 293.
[18] H.-W. Lin, J.-W. Chen, S. D. Cohen, and X. Ji, Flavor structure of the nucleon sea from lattice QCD, Phys. Rev. D **91**, 054510 (2015).
[19] J.-W. Chen, S. D. Cohen, X. Ji, H.-W. Lin, and J.-H. Zhang, Nucleon helicity and transversity parton distributions from lattice QCD, Nucl. Phys. **B911**, 246 (2016).
[20] C. Alexandrou, K. Cichy, V. Drach, E. Garcia-Ramos, K. Hadjiyiannakou, K. Jansen, F. Steffens, and C. Wiese, First results with twisted mass fermions towards the computation of parton distribution functions on the lattice, Proc. Sci., LATTICE2014 (**2014**) 135.
[21] C. Alexandrou, K. Cichy, V. Drach, E. Garcia-Ramos, K. Hadjiyiannakou, K. Jansen, F. Steffens, and C. Wiese, Lattice calculation of parton distributions, Phys. Rev. D **92**, 014502 (2015).
[22] H.-W. Lin, J.-W. Chen, T. Ishikawa, and J.-H. Zhang (LP3 Collaboration), Improved parton distribution functions at the physical pion mass, Phys. Rev. D **98**, 054504 (2018).
[23] H.-W. Lin *et al.*, Parton distributions and lattice QCD calculations: A community white paper, Prog. Part. Nucl. Phys. **100**, 107 (2018).
[24] M. Constantinou *et al.*, Parton distributions and lattice-QCD calculations: Toward 3D structure, Prog. Part. Nucl. Phys. **121**, 103908 (2021).
[25] R. Zhang, H.-W. Lin, and B. Yoon, Probing nucleon strange and charm distributions with lattice QCD, Phys. Rev. D **104**, 094511 (2021).
[26] A. Bazavov *et al.* (MILC Collaboration), Scaling studies of QCD with the dynamical HISQ action, Phys. Rev. D **82**, 074501 (2010).
[27] A. Bazavov *et al.* (MILC Collaboration), Lattice QCD ensembles with four flavors of highly improved staggered quarks, Phys. Rev. D **87**, 054505 (2013).
[28] I. W. Stewart and Y. Zhao, Matching the quasiparton distribution in a momentum subtraction scheme, Phys. Rev. D **97**, 054512 (2018).
[29] J.-W. Chen, T. Ishikawa, L. Jin, H.-W. Lin, Y.-B. Yang, J.-H. Zhang, and Y. Zhao, Parton distribution function with nonperturbative renormalization from lattice QCD, Phys. Rev. D **97**, 014505 (2018).
[30] X. Ji, Y. Liu, A. Schäfer, W. Wang, Y.-B. Yang, J.-H. Zhang, and Y. Zhao, A hybrid renormalization scheme for quasi light-front correlations in large-momentum effective theory, Nucl. Phys. **B964**, 115311 (2021).
[31] J.-W. Chen, L. Jin, H.-W. Lin, Y.-S. Liu, Y.-B. Yang, J.-H. Zhang, and Y. Zhao, Lattice calculation of parton distribution function from LaMET at physical pion mass with large nucleon momentum, arXiv:1803.04393.
[32] H.-W. Lin, J.-W. Chen, X. Ji, L. Jin, R. Li, Y.-S. Liu, Y.-B. Yang, J.-H. Zhang, and Y. Zhao, Proton Isovector Helicity Distribution on the Lattice at Physical Pion Mass, Phys. Rev. Lett. **121**, 242003 (2018).
[33] J.-H. Zhang, J.-W. Chen, L. Jin, H.-W. Lin, A. Schäfer, and Y. Zhao, First direct lattice-QCD calculation of the x-dependence of the pion parton distribution function, Phys. Rev. D **100**, 034505 (2019).
[34] J.-W. Chen, H.-W. Lin, and J.-H. Zhang, Pion generalized parton distribution from lattice QCD, Nucl. Phys. **B952**, 114940 (2020).
[35] S. Dulat, T.-J. Hou, J. Gao, M. Guzzi, J. Huston, P. Nadolsky, J. Pumplin, C. Schmidt, D. Stump, and C. P. Yuan, New parton distribution functions from a global analysis of quantum chromodynamics, Phys. Rev. D **93**, 033006 (2016).
[36] H.-L. Lai, M. Guzzi, J. Huston, Z. Li, P. M. Nadolsky, J. Pumplin, and C. P. Yuan, New parton distributions for collider physics, Phys. Rev. D **82**, 074024 (2010).
[37] P. M. Nadolsky, H.-L. Lai, Q.-H. Cao, J. Huston, J. Pumplin, D. Stump, W.-K. Tung, and C. P. Yuan, Implications of CTEQ global analysis for collider observables, Phys. Rev. D **78**, 013004 (2008).
[38] H. L. Lai, P. M. Nadolsky, J. Pumplin, D. Stump, W. K. Tung, and C. P. Yuan, The strange parton distribution of the nucleon: Global analysis and applications, J. High Energy Phys. 04 (2007) 089.
[39] F. Olness, J. Pumplin, D. Stump, J. Huston, P. M. Nadolsky, H. L. Lai, S. Kretzer, J. F. Owens, and W. K. Tung, Neutrino dimuon production and the strangeness asymmetry of the nucleon, Eur. Phys. J. C **40**, 145 (2005).
[40] D. Stump, J. Pumplin, R. Brock, D. Casey, J. Huston, J. Kalk, H. L. Lai, and W. K. Tung, Uncertainties of predictions from parton distribution functions. 1. The Lagrange multiplier method, Phys. Rev. D **65**, 014012 (2001).
[41] J. P. Berge *et al.*, A Measurement of differential cross-sections and nucleon structure functions in charged current neutrino interactions on iron, Z. Phys. C **49**, 187 (1991).
[42] W. G. Seligman *et al.*, Improved Determination of α_s from Neutrino Nucleon Scattering, Phys. Rev. Lett. **79**, 1213 (1997).
[43] J. C. Webb *et al.* (NuSea Collaboration), Absolute Drell-Yan dimuon cross-sections in 800 GeV/c pp and pd collisions, arXiv:hep-ex/0302019.
[44] J. Dove *et al.* (SeaQuest Collaboration), The asymmetry of antimatter in the proton, Nature (London) **590**, 561 (2021).
[45] H. Abramowicz *et al.* (H1, ZEUS Collaborations), Combination of measurements of inclusive deep inelastic $e^{\pm}p$ scattering cross sections and QCD analysis of HERA data, Eur. Phys. J. C **75**, 580 (2015).
[46] R. Aaij *et al.* (LHCb Collaboration), Measurement of the forward Z boson production cross-section in pp collisions at $\sqrt{s} = 7$ TeV, J. High Energy Phys. 08 (2015) 039.
[47] R. Aaij *et al.* (LHCb Collaboration), Measurement of forward $\mathrm{Z} \to \mathrm{e}^{+}\mathrm{e}^{-}$ production at $\sqrt{s} = 8$ TeV, J. High Energy Phys. 05 (2015) 109.
[48] V. Khachatryan *et al.* (CMS Collaboration), Measurement of the differential cross section and charge asymmetry for inclusive $\mathrm{pp} \to \mathrm{W}^{\pm} + X$ production at $\sqrt{s} = 8$ TeV, Eur. Phys. J. C **76**, 469 (2016).

[49] R. Aaij *et al.* (LHCb Collaboration), Measurement of forward W and Z boson production in pp collisions at $\sqrt{s} = 8$ TeV, J. High Energy Phys. 01 (2016) 155.
[50] V. M. Abazov *et al.* (D0 Collaboration), Measurement of the muon charge asymmetry from W boson decays, Phys. Rev. D **77**, 011106 (2008).
[51] S. Chatrchyan *et al.* (CMS Collaboration), Measurement of the muon charge asymmetry in inclusive $pp \to W + X$ production at $\sqrt{s} = 7$ TeV and an improved determination of light parton distribution functions, Phys. Rev. D **90**, 032004 (2014).
[52] S. Chatrchyan *et al.* (CMS Collaboration), Measurement of the Electron Charge Asymmetry in Inclusive W Production in pp Collisions at $\sqrt{s} = 7$ TeV, Phys. Rev. Lett. **109**, 111806 (2012).
[53] V. M. Abazov *et al.* (D0 Collaboration), Measurement of the electron charge asymmetry in $\boldsymbol{p\bar{p} \to W + X \to e\nu + X}$ decays in $\boldsymbol{p\bar{p}}$ collisions at $\sqrt{\boldsymbol{s}} = \mathbf{1.96}$ TeV, Phys. Rev. D **91**, 032007 (2015); **91**, 079901(E) (2015).
[54] E. L. Berger, J. Gao, C. S. Li, Z. L. Liu, and H. X. Zhu, Charm-Quark Production in Deep-Inelastic Neutrino Scattering at Next-to-Next-to-Leading Order in QCD, Phys. Rev. Lett. **116**, 212002 (2016).
[55] C. Alexandrou, S. Bacchio, M. Constantinou, J. Finkenrath, K. Hadjiyiannakou, K. Jansen, G. Koutsou, H. Panagopoulos, and G. Spanoudes, Complete flavor decomposition of the spin and momentum fraction of the proton using lattice QCD simulations at physical pion mass, Phys. Rev. D **101**, 094513 (2020).
[56] Y.-B. Yang, J. Liang, Y.-J. Bi, Y. Chen, T. Draper, K.-F. Liu, and Z. Liu, Proton Mass Decomposition from the QCD Energy Momentum Tensor, Phys. Rev. Lett. **121**, 212001 (2018).
[57] C. Schmidt, J. Pumplin, C. P. Yuan, and P. Yuan, Updating and optimizing error parton distribution function sets in the Hessian approach, Phys. Rev. D **98**, 094005 (2018).
[58] T.-J. Hou, Z. Yu, S. Dulat, C. Schmidt, and C. P. Yuan, Updating and optimizing error parton distribution function sets in the Hessian approach. II., Phys. Rev. D **100**, 114024 (2019).
[59] J. Pumplin, D. R. Stump, J. Huston, H. L. Lai, P. M. Nadolsky, and W. K. Tung, New generation of parton distributions with uncertainties from global QCD analysis, J. High Energy Phys. 07 (2002) 012.
[60] L. A. Harland-Lang, A. D. Martin, P. Motylinski, and R. S. Thorne, Uncertainties on α_S in the MMHT2014 global PDF analysis and implications for SM predictions, Eur. Phys. J. C **75**, 435 (2015).
[61] R. S. Towell *et al.* (NuSea Collaboration), Improved measurement of the $\bar{d}/\bar{u}$ asymmetry in the nucleon sea, Phys. Rev. D **64**, 052002 (2001).
[62] T.-J. Hou, M. Yan, J. Liang, K.-F. Liu, and C. P. Yuan, Connected and disconnected sea partons from the CT18 parametrization of PDFs, Phys. Rev. D **106**, 096008 (2022).
[63] A. M. Sirunyan *et al.* (CMS Collaboration), Measurement of associated production of a W boson and a charm quark in proton-proton collisions at $\sqrt{s} = 13$ TeV, Eur. Phys. J. C **79**, 269 (2019).
[64] G. Aad *et al.* (ATLAS Collaboration), Measurement of the production of a W boson in association with a charm quark in pp collisions at $\sqrt{s} = 7$ TeV with the ATLAS detector, J. High Energy Phys. 05 (2014) 068.
[65] S. Chatrchyan *et al.* (CMS Collaboration), Measurement of associated $\mathrm{W} + \mathrm{charm}$ production in pp collisions at $\sqrt{s} = 7$ TeV, J. High Energy Phys. 02 (2014) 013.
[66] O. Samoylov *et al.* (NOMAD Collaboration), A precision measurement of charm dimuon production in neutrino interactions from the NOMAD experiment, Nucl. Phys. **B876**, 339 (2013).
[67] A. Buckley, J. Ferrando, S. Lloyd, K. Nordström, B. Page, M. Rüfenacht, M. Schönherr, and G. Watt, LHAPDF6: Parton density access in the LHC precision era, Eur. Phys. J. C **75**, 132 (2015).
[68] T.-J. Hou, P. Nadolsky, K. Xie, and C.-P. Yuan, CTEQ-TEA Hepforge, https://ct.hepforge.org.
[69] R. G. Edwards and B. Joo (SciDAC, LHPC, UKQCD Collaborations), The Chroma software system for lattice QCD, Nucl. Phys. B, Proc. Suppl. **140**, 832 (2005).